# Experimental and Numerical Investigation on the Performance of a Moored Pitching Wave Energy Conversion System

Bruno Paduano, Fabio Carapellese, Edoardo Pasta, *Graduate Student Member, IEEE*, Mauro Bonfanti, Sergej Antonello Sirigu, Dario Basile, Domenica Pizzirusso, Nicoláas Faedo, and Giuliana Mattiazzo

***Abstract*—This study delves into the question of whether the mooring system influences the dynamics of the device by conducting a comprehensive analysis of the inertial sea wave energy converter (ISWEC). Recognizing that wave energy converters exhibit complex behaviors that often push numerical models beyond their range of validity, this study highlights the importance of developing a representative model that accurately captures the intricate dynamics involved. To address this challenge, an experimental investigation of the ISWEC is conducted, aiming to establish a benchmark model that serves as a reference for validating and refining numerical models. Following the experimental investigation, this study proceeds with a numerical investigation to further explore the influence of the mooring system on the pitching device. The response of the device is analyzed both with and without the mooring system, allowing for a direct comparison of its effects on device dynamics and the associated harvested energy. By conducting numerical simulations under various operating conditions, this study provides an insight into the definition of representative mathematical modeling, analyzing and motivating the strong influence of the mooring system on the performances of a moored pitching wave energy conversion system.**

***Index Terms*—Experimental validation, inertial sea wave energy converter (ISWEC), mooring system, wave energy converter (WEC) performances, wave energy.**

## I. Introduction

In THE past decades, in light of the sustainable development goals [1], governments have been pushing to mitigate global pollution by exploiting renewable energy sources. Wave energy, in particular, holds significant potential in shaping the future energy landscape [2]. While photovoltaic and wind technologies have gained traction in the current energy market [3], [4], [5], wave energy conversion systems are still in the developmental stage [6]. Therefore, further research is crucial to effectively commercialize these technologies.

During the development of novel technologies such as wave energy systems, the use of experimental data plays a vital role in assessing their potential and validating associated mathematical models [7]. The validation process is essential to assess the limits of both technologies and mathematical models. Especially in the wave energy field, the behavior of wave energy systems pushes the commonly adopted numerical model [such as the linear boundary element method (BEM)-based models] outside the range of validity imposed by the assumptions [8]. Furthermore, the scaling of a device limits the applicability and the use of the corresponding energy-harvesting mechanism, since on a small scale, especially the friction-related phenomena are predominant [9] and the response of a mechanism can be nonrepresentative. Hence, mostly, wave energy systems are generally scaled and analyzed experimentally by omitting, or simplifying, the corresponding mechanism [10], [11].

During the development of novel technologies such as wave energy systems, the use of experimental data plays a vital role in assessing their potential and validating associated mathematical models [7]. The validation process is essential to determine the limits of both the technologies and the mathematical models. In the field of wave energy, the complex behavior of wave energy systems often pushes commonly used numerical models, such as linear BEM-based models, beyond their range of validity due to underlying assumptions [8]. Additionally, scaling a device for experimental analysis can introduce limitations in the applicability of the corresponding energy-harvesting mechanism. In small-scale experiments, phenomena related to friction become predominant and the response of the mechanism may not be representative [9]. Within this general picture, floating offshore wave energy systems are station-kept by means of mooring systems. Ideally, a mooring system needs to be able to guarantee the device survivability influencing as little as possible the associated device response and, hence, the power extraction. Clearly, in real applications, the influence of mooring systems on the device productivity has been studied numerically, finding that moorings can play a fundamental role in the device dynamics [12], [13], [14], [15], [16], [17], [18].

Manuscript received 30 August 2023; revised 22 November 2023; accepted 6 January 2024. Date of publication 18 March 2024; date of current version 16 July 2024. *(Corresponding author: Bruno Paduano.)*

**Associate Editor: K. Takagi.**

Bruno Paduano, Fabio Carapellese, Edoardo Pasta, Mauro Bonfanti, Sergej Antonello Sirigu, Nicoláas Faedo, and Giuliana Mattiazzo are with the Mechanical and Aerospace Department (DIMEAS), Politecnico di Torino, 10128 Turin, Italy (e-mail: bruno.paduano@polito.it; fabio.carapellese@polito.it; edoardo.pasta@polito.it; mauro.bonfanti@polito.it; sergej.sirigu@polito.it; nicolas.faedo@polito.it; giuliana.mattiazzo@polito.it).

Dario Basile is with the Eni S.P.A., 20097 San Donato Milanese, Italy (e-mail: dario.basile2@eni.com).

Domenica Pizzirusso is with the EniProgetti S.p.A., San Donato Milanese, 20097, Italy (e-mail: domenica.pizzirusso@eni.com).

Digital Object Identifier 10.1109/JOE.2024.3353372

Among the various wave energy technologies, this study focuses on the inertial sea wave energy converter (ISWEC). The ISWEC is a pitching wave energy converter (WEC) that harnesses energy through a gyroscopic internal mechanism (see Section II for more information). The device under investigation has been prototyped and analyzed experimentally. Furthermore, it is a fully-equipped device that includes the energy conversion mechanism, the behavior of which is characterized empirically.

### A. Aims and Contributions

This study aims to validate a comprehensive moored model of the ISWEC, which includes all the essential components: the mooring system that is responsible for solving the station-keeping problem, the hull that defines the wave–structure interaction and the device hydrodynamics, and the energy conversion mechanism with its corresponding control strategy. The aim is to shed light on the modeling limitation of the ISWEC and analyze the influence and impact of the mooring system on the overall system performance. To achieve this, a numerical investigation is conducted using the validated model.

The first part of this study focuses on the experimental investigation of the ISWEC, which was conducted in 2021 at the facilities of the Università Federico II in Naples. The tests aimed to reproduce a significant number of operational irregular waves to simulate real site conditions and accurately characterize the device's response. The experimental campaign and, consequently, the validation are scheduled and divided into three parts, which are as follows:

1) motion: validation of the uncontrolled device subject to the mooring influence;
2) mechanism: validation of the whole model including the mechanical part;
3) mooring: validation of the mooring tensions.

Consequently, in the second part of this study, to assess the impact of the mooring system on the system dynamics, a numerical investigation is conducted by comparing the validated model with mooring to the unmoored model. This investigation focuses on site scatter, specifically the Pantelleria scatter. Initially, the comparison is performed under free motion (uncontrolled) conditions, solely examining the discrepancies in the device motion while disregarding the influence of the mechanical system. Furthermore, the analysis incorporates the mechanism and its associated controller to evaluate the differences between the device design conditions (unmoored) and its actual real-world counterpart (moored). The controller synthesis for the ISWEC prototype was performed by utilizing the empirical transfer function estimate of the controlled system. This approach allowed for a straightforward and efficient assessment of the control action, even during the experimental campaign, by employing the impedance-matching technique. This methodology enabled a quick evaluation of the controller's performance and effectiveness, providing valuable insights into the control strategy of the ISWEC.

The rest of the article is organized as follows: In Section II, the device under investigation is presented. The mathematical models and the related assumptions on which these models are based are debated in Section III. In Section IV, the experimental campaign is presented. In Section V, the model validation is exposed and discussed. The numerical discussion on the influence of the mooring system is placed in Section VI. Finally, Section VII concludes this article.

Note that, within this article, several variables are expressed in a dimensionless form, see Remark 1, for further information.

*Remark 1:* This study is based on a commercial investigation of the technology ISWEC founded by ENI S.P.A.; hence, the following variables are omitted or expressed in a dimensionless form to avoid any confidentiality issue.

1) Frequency: Expressed as $\omega/\omega_r$, being $\omega_r$ the pitch resonant frequency of the hull.
2) Physical properties: Geometry, inertial properties of the device and its mooring system, and the prototype associate scaling factor are omitted.

Although the study presented here is based on a validation conducted using a dimensionless form of several variables (see Remark 1), it is important to note that the mathematical model itself is constructed in a full-scale context. The validation process involved scaling up the *responses* of the prototype to align with the full-scale model. This approach is taken to ensure that both parts of this study utilize the same mathematical model and incorporate real-scale environmental data directly into the analysis.

### B. Notation

$\mathbb{R}^+$ is used to represent the set of positive real numbers. $F(\omega) = \mathcal{F}(f(t))$ represents the Fourier transform of the function $f$. Moreover, whenever a function is represented with a Greek letter, its Fourier transform is indicated as $\tilde{\eta}$.

Being a matrix $A \in \mathbb{C}^{n\times m}$, $A^* \in \mathbb{C}^{m\times n}$ represents the Hermitian of $A$. Additionally, given a square nonsingular matrix $B$, $B^{-*}$ denotes the inverse Hermitian of $B$. Being a matrix $A \in \mathbb{C}^{n\times m}$, $A_{i,j} \in \mathbb{C}$ represents the element of the matrix $A$ defined by means of the indices $i, j$ with $i \in \{1, \ldots, n\}$ and $j \in \{1, \ldots, m\}$.

## II. Inertial Sea Wave Energy Converter

Within this section, the working principle of the ISWEC, the device under investigation, is described. The ISWEC is a floating offshore wave energy system composed of a monolithic hull, which is able to protect the mechanism, responsible for the energy extraction, from the hostile marine environment. The internal mechanism is formed by two gyroscopes, each rotating around the power take-off (PTO) axis $\varepsilon$. The rotation is induced by the combined action of pitch $z_5$, wave-induced motion, and gyroscopic torque generated by the flywheel rotation around its own axis $\varphi$. Each flywheel rotates with an opposite speed, and the associated gyroscopic axis is in antiphase. The opposite precession movement is induced by design to reduce the undesired effect on the hull (e.g., reaction forces on roll motion, among others [19]).

A representation of the ISWEC working principle is exposed in Fig. 1. Note that, following the discussion immediately above, the ISWEC can be defined as a pitching wave energy system, since the pitch motion is linked to the rotation of the $\varepsilon$-axis and, hence, directly to power extraction.

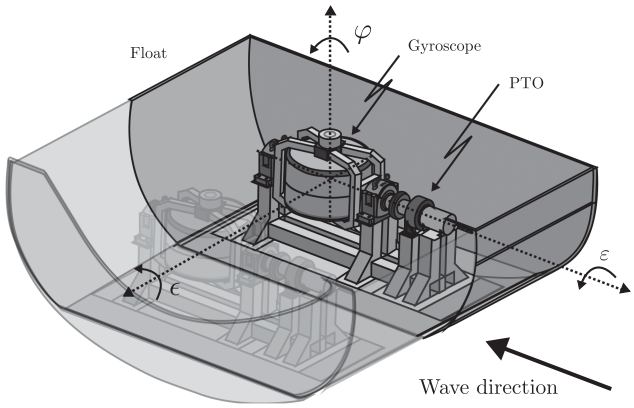


Fig. 1. ISWEC working principle.

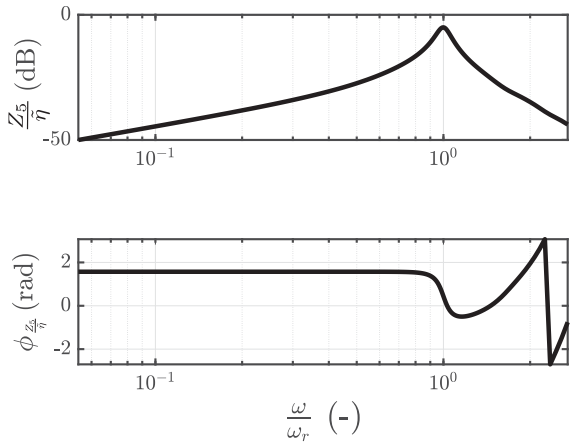


Fig. 2. ISWEC pitch RAO ($Z_5/\tilde{\eta}$ map).

## III. Numerical Modeling

Since within this study, the validation of the ISWEC mathematical models is presented and analyzed accordingly, a detailed analysis of such models, is presented within this section. In particular, we begin by noting that a floating offshore wave energy system is essentially formed by three main components, that is, 1) the mooring system, responsible for solving the station-keeping problem, 2) the mechanical system, responsible for the energy conversion process, and 3) the device hull and associated shape, which are directly related to fluid–structure interactions. In the following, and based on the previous description, a (nonlinear) time-domain derivation of the models associated with each component of the WEC system is presented.

The equation of motion of the device is solved by means of the numerical solver OrcaFlex (OF) [20], a commercial software widely used in the offshore field [21]. The hydrodynamic model is based on the well-known assumptions described by the so-called potential flow theory [22], which can be represented in terms of a Volterra integro-differential equation of the convolution type [23], i.e.

$$(m+m_\infty)\ddot{z}(t)+\int_{-\infty}^{t} h_r(\tau)\dot{z}(t-\tau)\mathrm{d}\tau+h_k z(t) = f_w(t)-f_{\text{gyro}}(t)-f_m(t) \quad (1)$$

in which $\{m, m_\infty, h_k\} \subset \mathbb{R}^{6\times 6}$ represent the inertia, added mass, and hydrostatic stiffness matrix of the device, respectively, $h_r : \mathbb{R}^+ \to \mathbb{R}^6, t \mapsto h_r(t)$ is the radiation impulse response function, and $z : \mathbb{R}^+ \to \mathbb{R}^6, t \mapsto z(t)$ is the device motion. Finally,

$$\{f_w, f_{\text{gyro}}, f_m\} : \mathbb{R}^+ \to \mathbb{R}^6, \quad t \mapsto \{f_w(t), f_{\text{gyro}}(t), f_m(t)\}$$

are the wave forces, divided into wave first-order excitation force and drift forces, the mechanical force applied by the gyroscopic system, and the mooring force, respectively.

Based on (1), it is possible to appreciate the integration of the following nonlinear effects.

1) Wave force: The excitation force on the hull is evaluated by including second-order terms (slow varying forces) defined as in [22], in particular, $f_w = f_e + f_{\text{drift}}$.
2) Mooring force: The mooring problem is solved by means of OF, which represents the mooring system in a dynamic lumped-mass fashion [20].
3) Mechanism force: The integration of the mechanism and the associated control (gyroscopes and PTO system) is achieved by compiling the electromechanical part, described by means of a Simulink model, in C++ code and, consequently, converted in a dynamic library to ensure the real-time communication with the master software, i.e., OF. The whole process is described in [15]. The specific equations, characterizing such a mechanism, are described within this article, in Section III-A.

Although the model leverages a 6-DoF representation, the pendulum equations are derived in a 3-DoF model, and hence, only effects on surge, heave, and pitch motion are considered [15].

The hydrodynamic properties are evaluated by means of BEM software, that is, within this study, the software provided by Orcina and naturally coupled with OF, i.e., OrcaWave (OW). In detail, and with reference to Fig. 3, the properties evaluated by dint of BEM are relative to the maps $\Sigma_{f_e}$, $\Sigma_{f_{\text{drift}}}$, and $\Sigma_d$ (as described in the following paragraphs). If nonlinear effects are neglected, i.e., we simply consider the hydrodynamic behavior of the ISWEC, the device motion can be described in terms of an input/output (I/O), wave-to-motion (w2m) system, by means of the so-called response amplitude operator (RAO). By way of example, in Fig. 2, the device pitch RAO is exposed.

Note that the overall system is presented, leveraging a schematic fashion, in Fig. 3, highlighting any nonlinear effects. According to (1), it is possible to define: $\{\Sigma_{f_e}, \Sigma_{f_{\text{drift}}}\} : \mathbb{R} \to \mathbb{R}^6$ as the linear and nonlinear map related to wave forces ($f_e$ and $f_{\text{drift}}$, respectively), $\{\Sigma_{\text{moor}}, \Sigma_{\text{gyro}}\} : \mathbb{R}^6 \to \mathbb{R}^6$ as the mooring and gyroscopic representation, and, finally, $\Sigma_d : \mathbb{R}^6 \to \mathbb{R}^6$ as the linear map associated with the device hydrodynamics. $K_{fb} : \mathbb{R}^2 \to \mathbb{R}^2$ is the controller that drives the mechanical system.

### A. Mechanism and Control

The system mechanism, together with the corresponding frame of references (FoR), is reported in Fig. 4. FoRs represented

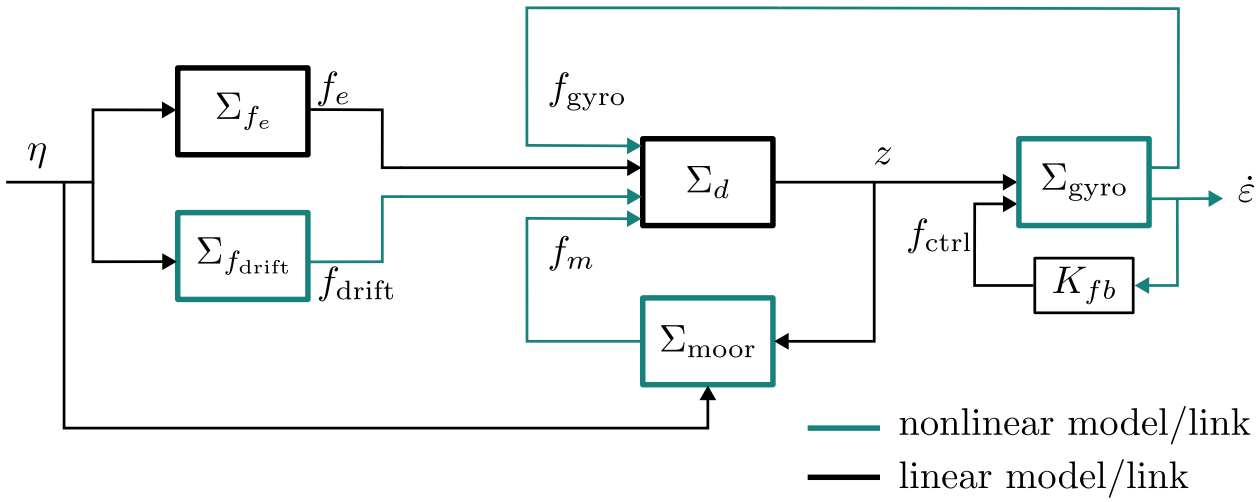


Fig. 3. ISWEC block representation. The nonlinearities are highlighted in green. Note that variables are expressed in the time domain.

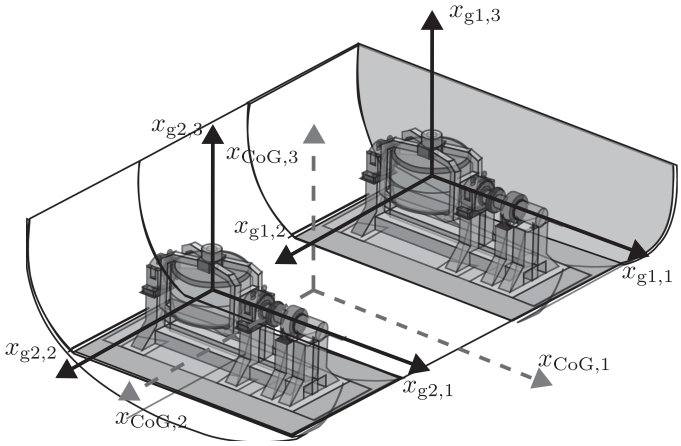


Fig. 4. ISWEC and associated mechanism FoRs.

with black solid lines are mobile frames of references fixed on the gyroscopic units and are free to rotate around the $x_{gi,1}$-axis, with $i \in \{1, 2\}$. The FoR represented with dashed lines is referred to the ISWEC system, with the origin in the device's center of gravity (CoG).

The nonlinear equation, which describes the force balance at the $\varepsilon$-axis, for each gyroscope, is

$$\begin{aligned} f_\varepsilon = {} & m_{fw,4,4}\dot{z}_5\dot{\varphi}\cos(\varepsilon) - f_{\text{ctrl}} - m_{p,1,1}gl\sin(\varepsilon) \\ & - (m_{fw,6,6} - m_{fw,5,5})\dot{z}_5^2\sin(\varepsilon)\cos(\varepsilon) \\ & + m_{fw,6,6}\dot{\varphi}\dot{z}_5\cos(\varepsilon) \end{aligned} \tag{2}$$

in which $\{\varepsilon, f_{\text{ctrl}}, f_\varepsilon\} : \mathbb{R} \to \mathbb{R}, t \mapsto \{\varepsilon(t), f_{\text{ctrl}}(t), f_\varepsilon(t)\}$ represent the PTO axis rotation, the control torque, and the total torque on the $\varepsilon_i$-axis, respectively. Moreover, $\dot{\varphi}(t) \subset \mathbb{R}^+$ is the constant[1] flywheel speed. The overall gyroscopic system can be physically represented by three main components, which are as follows.

1) A structure, fixed to the device.
2) A pendulum, which is free to rotate around $x_{gi,1}$-axis.
3) A flywheel, which rotates, together with the pendulum, about $x_{gi,1}$-axis, with constant speed $\dot{\varphi}$ about the mobile vertical axis.

Accordingly, $\{m_s, m_{fw}, m_p\} \subset \mathbb{R}^{6\times6}$ describe the inertia properties of the structure, flywheel, and pendulum, respectively. These matrices are referred to as the associated principal body frames, i.e., are diagonal. $l \in \mathbb{R}^+$ represents the vertical distance of the pendulum CoG to the mechanism FoR.

The gyroscopic equations and associated motions are derived according to 3 DoFs, i.e., surge, heave, and pitch, with respect to the hull FoR. Accordingly, the forces applied on the hull CoG by the mechanism are

$$f_{\text{gyro}} = \begin{bmatrix} f_{\text{gyro},1} & 0 & f_{\text{gyro},3} & 0 & f_{\text{gyro},5} & 0 \end{bmatrix}^\intercal \tag{3}$$

in which

$$\begin{aligned} f_{\text{gyro},1} = {} & (m_{s,1,1} + m_{fw,1,1} + m_{p,1,1})(\ddot{z}_1 + d_0\ddot{z}_5) \\ & - m_{p,1,1}l\ddot{z}_5\cos(\varepsilon) + 2m_{p,1,1}l\dot{\varepsilon}\dot{z}_5\sin(\varepsilon) \\ & + (m_{s,1,1} + m_{fw,1,1} + m_{p,1,1})\dot{z}_1\dot{z}_5 \\ f_{\text{gyro},3} = {} & (m_{s,1,1} + m_{fw,1,1} + m_{p,1,1})\ddot{z}_3 \\ & - (m_{s,1,1} + m_{fw,1,1} + m_{p,1,1})\dot{z}_5\dot{z}_1 \\ & - (m_{s,1,1} + m_{fw,1,1} + m_{p,1,1})\ddot{z}_5^2 d_0 + m_{p,1,1}l\dot{z}_5^2\cos(\varepsilon) \\ & + m_{p,1,1}l\dot{\varepsilon}^2\cos(\varepsilon) + m_{p,1,1}l\ddot{\varepsilon}\sin(\varepsilon) \\ f_{\text{gyro},5} = {} & ((m_{s,1,1} + m_{fw,1,1} + m_{p,1,1})d_0 - m_{p,1,1}l\cos(\varepsilon))\ddot{z}_1 \\ & - m_{fw,6,6}\ddot{\varphi}\sin(\varepsilon) \\ & + ((m_{s,5,5} + m_{fw,5,5} + m_{p,5,5} + m_{p,1,1}l^2)\cos^2(\varepsilon) \\ & + (m_{s,6,6} + m_{fw,6,6} + m_{p,6,6})\sin^2(\varepsilon) \end{aligned}$$

[1]Note that, although the flywheel velocity is constant in time, it changes according to the sea state to maximize the extracted energy. For further details, the reader can refer to the work in [24].

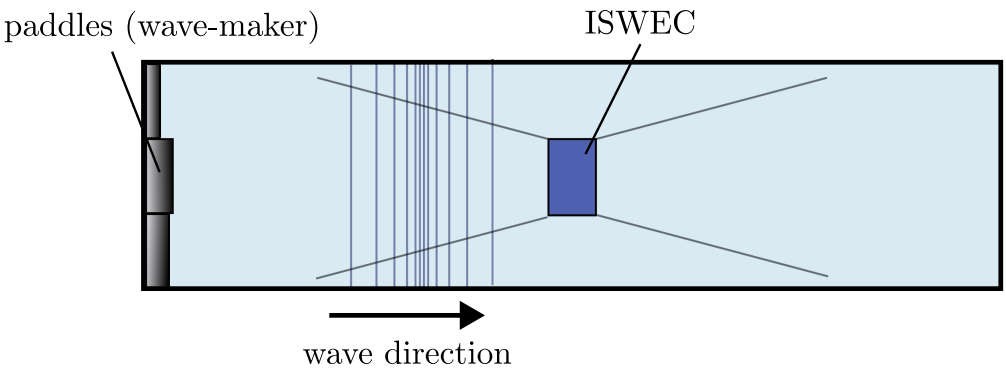


Fig. 5. Schematic representation of the wave basin.

$$
\begin{aligned}
&+(m_{s,1,1}+m_{fw,1,1}+m_{p,1,1})d_0^2-2m_{p,1,1}d_0\\
&\times\cos(\varepsilon))\ddot{z}_5+(2(m_{s,6,6}+m_{fw,6,6}+m_{p,6,6})\\
&-2(m_{s,5,5}+m_{fw,5,5}+m_{p,5,5}+m_{p,1,1}l^2))\dot{\varepsilon}\dot{z}_5\\
&\times\sin(\varepsilon)\cos(\varepsilon)+2m_{p,1,1}l\dot{\varepsilon}\dot{z}_5\sin(\varepsilon)d_0\\
&+((m_{s,1,1}+m_{fw,1,1}+m_{p,1,1})d_0-m_{p,1,1}l\cos(\varepsilon))\dot{z}_5\dot{z}_3\\
&-m_{fw,6,6}\dot{\varphi}\dot{\varepsilon}\cos(\varepsilon)+mlg\cos^2(\varepsilon)\sin(z_5) \qquad (4)
\end{aligned}
$$

where $d_0$ represents the distance of $x_{\text{CoG},3}$ on the mechanism FoR.

Finally, the extracted energy $L$, by both gyroscopic units, can be defined, over a certain time interval $\Delta t=[t_1,t_2]$, as

$$
L=\frac{1}{t_2-t_1}\int_{t_1}^{t_2}\left(f_{\text{ctrl},1}(t)\dot{\varepsilon}_1(t)+f_{\text{ctrl},2}(t)\dot{\varepsilon}_2(t)\right)\mathrm{d}t. \qquad (5)
$$

## IV. Experimental Campaign

In this section, the experimental tests performed are detailed and discussed.

### A. Facilities and Acquisition System

The experimental campaign has been carried out within the facilities of the *Università degli studi di Napoli Federico II* in Naples, Italy. The laboratory towing tank's overall dimensions are $135\,\text{m}\times 9\,\text{m}\times 4.2\,\text{m}$ (length, width, and depth, respectively). The facility integrates wave capacity gauges to measure wave elevation and a Qualisys optical motion tracking system to acquire floater motion. Moreover, the device is provided with the following instrumentation:

1) onboard computer system, for data acquisition and control implementation.
2) inertial measurement unit, for measurement of the floater kinematics.
3) four load cells, to acquire mooring tension at the fairleads.
4) torque sensor and encoder, to measure PTO axis force and motion.

In Fig. 5, a schematic representation of the wave tank facility is exposed. Since the wave basin has a prevalent dimension (i.e., a *flume*), the ISWEC is excited only on surge, heave, and pitch motions.

### B. Prototype Gyroscopes: Friction Identification

Real systems introduce friction effects due to the contact between mechanical components. This is clearly the case for the gyroscope system, whose $\varepsilon$-axis is coupled with a gearbox and then supported by a set of radial roller bearings, which allows the precession rotation of the gyroscopic system. With the purpose of providing an experimental representation of these effects, we present, within this section, a set of tests performed in the hardware-in-the-loop system for the gyroscopic mechanism. Such tests are a fundamental characterization of the friction force. In particular, let us define the system $\Sigma_f:\mathbb{R}^+\to\mathbb{R}$, which describes the dynamics of the precession axis, considering the parametric excitation due to the pitch rotation $z_5$, exclusively. In particular, the equation is computed as follows:

$$
\begin{aligned}
\Sigma_f:\ f_\varepsilon &= m_{fw,4,4}\dot{z}_5\dot{\varphi}\cos(\varepsilon)-f_{\text{ctrl}}-m_{p,1,1}gl\sin(\varepsilon)\\
&-(m_{fw,6,6}-m_{fw,5,5})\dot{z}_5^2\sin(\varepsilon)\cos(\varepsilon)\\
&+m_{fw,6,6}\dot{\varphi}\dot{z}_5\cos(\varepsilon)+T_f \qquad (6)
\end{aligned}
$$

where the friction torque $T_f$ is added to (2). As previously mentioned, the gyroscope-electric generator coupling involves a gear stage in between; hence, the most suitable model, characterizing the dissipative effects arising from such transmission stages, is the Stribeck friction model [25]. This model describes the friction torque $\dot{\varepsilon}\mapsto T_f$, as a function of several friction effects, with a corresponding impact depending on the precession velocity $\dot{\varepsilon}$, as shown in Fig. 6.

In particular, knowing that the Stribeck friction $T_s(t)\in\mathbb{R}$ corresponds with the negative slope at low velocities, the complete mathematical expression of the friction torque is as follows [25]:

$$
T_f=(T_{\text{brk}}-T_c)e^{-\left(\frac{\dot{\varepsilon}}{\omega_{\text{st}}}\right)^2}+T_c\tanh\left(\frac{\dot{\varepsilon}}{\omega_{\text{coul}}}\right)+T_v \qquad (7)
$$

where terms of (7) are as follows.

1) The Coulomb friction $T_c$ results in a constant force at any velocity.
2) The viscous friction $T_v=c_v\dot{\varepsilon}$ is directly proportional to the relative velocity.
3) The breakaway friction $T_{\text{brk}}$ is defined as the sum of the Coulomb and Stribeck frictions at the vicinity of zero velocity.

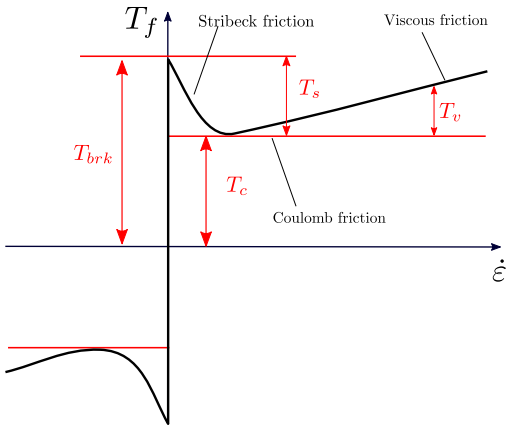


Fig. 6. Characterization of the Stribeck friction function.

TABLE I
VALUE OF THE IDENTIFIED FRICTION PARAMETERS

| Parameter | Unit | Value |
|---|---|---|
| $T_c$ | N·m | 0.012 |
| $T_{\text{brk}}$ | N·m | 0.022 |
| $\omega_{\text{brk}}$ | rad/s | 0.065 |
| $c_v$ | N·m·s/rad | 0.0046 |

4) The Stribeck velocity threshold $\omega_{\text{st}} = \omega_{\text{brk}}\sqrt{2}$.
5) The Coulomb velocity threshold $\omega_{\text{coul}} = \omega_{\text{brk}}/10$.

On the basis of this, several experimental tests have been performed to identify the right friction function for the scaled ISWEC system. In particular, the gyroscope precession rotation $\varepsilon$ has been measured, forcing a parametric excitation on the system, generated by a suitably designed $z_5$ signal, as detailed in the following paragraphs. The pitch motion is generated via a Stewart platform, on which the gyroscope is mounted. Note that all the tests are performed with no control action applied, i.e., $f_{\text{ctrl}} = 0 \forall t$.

Therefore, the experimental tests are designed to impose as input a regular pitch motion, varying the signal amplitude at different flywheel velocities $\dot{\varphi}$. Furthermore, the input harmonic signals are considered at different frequencies according to the operational range of the gyroscope. The output measured is the precession oscillation of the gyroscope. Through the knowledge of the imposed input signal $z_5$ and the measured signal $\varepsilon$, the friction parameters are estimated via system identification routines. The identified parameters are reported in Table I, and the function $T_f$ characterizing the ISWEC friction is presented in Fig. 7.

*Remark 2:* Note that the gyroscopic friction is identified through an averaging process since tests are performed at several amplitude conditions of the system input $z_5$.

### C. Validation Stages

Although the overall purpose is already defined, in this section, the aim of the experimental campaign is eviscerated and discussed. According to the block diagram exposed in Fig. 3 and

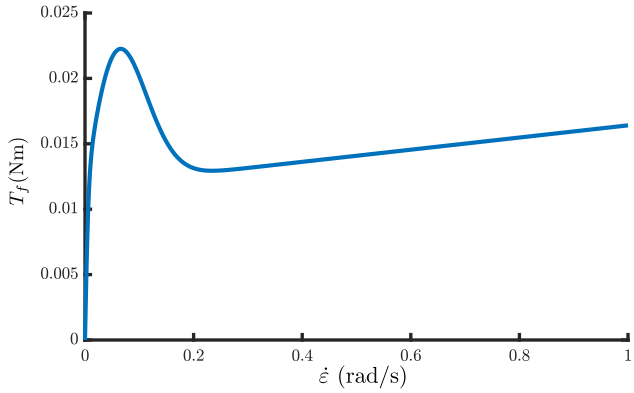


Fig. 7. Representation of the mathematical function for the friction characterization of the ISWEC system.

the acquisition system available, the following validation stages are pursued.

1) w2m: Within this stage, the mathematical model representing the device motion is tested. Note that, within these tests, the gyroscopic units are in safety mode, *i.e.*, mechanically blocked.
2) w2g: Being the aim of a wave energy device, a fundamental role of the experimental campaign is played by this validation stage, where, the overall system is effectively tested, including a corresponding control action applied via the PTO system.
3) w2t: A floating structure needs to be moored and tested in extreme conditions, accordingly. Since nonlinearities can be enhanced due to the large motions induced during these events, an experimental validation is requested by standard [26], and, hence, a statistical validation process is proposed accordingly.

### D. Test Matrix

The ISWEC is a device designed to operate in the Mediterranean Sea [27], [28]. The site selected to define the waves for the experimental campaign is Pantelleria, Sicily, in the southern part of Italy. The irregular waves selected to be reproduced within the wave tank are selected from the Pantelleria corresponding environmental scatter to pick a sufficiently large set of representative waves. The selected waves are reported in Table II, already divided according to the validation purpose. Apart from the operative, scatter-picked, irregular waves, an extremely irregular sea state is chosen to assess the model within a strongly nonlinear condition. Note that, the methodology used to assess the extreme environmental conditions is defined in [29].

### E. Prototype and Mooring System

Within this section, a brief description of the ISWEC prototype, the associated mechanism, and its mooring system is provided.

The complete system is developed through a comprehensive full-scale design process that utilizes an appropriate optimization algorithm [24], [30]. To ensure that the prototype accurately represents the characteristics of a fully optimized full-scale

TABLE II
WAVES LIST, DIVIDED ACCORDING TO VALIDATION STAGE/OBJECTIVES, I.E., W2M, W2T, AND W2G

| Wave identifier | $T_e$ $(s)$ | $H_s$ $(m)$ | w2m | w2t | w2g |
|---|---|---|---|---|---|
| 01 irr | 5 | 1.3 | ◯ | | ◯ |
| 02 irr | 6 | 1.86 | ◯ | | |
| 03 irr | 7 | 2.55 | ◯ | | |
| 04 irr | 4.5 | 1.05 | ◯ | | ◯ |
| 05 irr | 5.5 | 1.57 | ◯ | | ◯ |
| 06 irr | 6.5 | 2.2 | ◯ | | |
| 07 irr | 7 | 2.93 | ◯ | | |
| 08 irr | 7.5 | 1.76 | ◯ | | |
| 09 irr | 8 | 2 | ◯ | | |
| 10 ext | 3.45 | 6 | ◯ | ◯ | |

TABLE III
PROTOTYPE SCALING LAW

| ISWEC device | | |
|---|---|---|
| Parameter | unit | Froude's scale factor |
| hull length | m | $\lambda$ |
| hull width | m | $\lambda$ |
| hull height | m | $\lambda$ |
| CoG $x_3$ position | m | $\lambda$ |
| draft | m | $\lambda$ |
| pitch inertia moment | kg.m$^2$ | $\lambda^5$ |
| roll inertia moment | kg.m$^2$ | $\lambda^5$ |
| yaw inertia moment | kg.m$^2$ | $\lambda^5$ |
| device mass | kg | $\lambda^3$ |
| **Gyroscopic units** | | |
| flywheel inertia moment | kg.m$^2$ | $\lambda^5$ |
| generator nominal power | kW | $\lambda^{3.5}$ |
| generator nominal torque | N.m | $\lambda^4$ |
| generator nominal speed | r/min | $\lambda^{-0.5}$ |

device, Froude's law is applied, which establishes a proportional relationship between the physical characteristics of the prototype, and the corresponding features of the full-scale system. By adhering to Froude's law, the scale factor specified in Table III is employed to determine the appropriate dimensions and properties of the prototype. This scaling methodology guarantees that the prototype faithfully captures the relevant dynamics and behavior exhibited by the full-scale system, thereby providing valuable insights and data for further analysis and development.

As previously discussed within Section II, the floater is composed of a steel hull that encloses two gyroscopic units, as illustrated in Fig. 8. It is worth noting that each gyroscopic unit is equipped with an encoder that accurately detects and measures the angular position of the gyroscopic axis. The encoder is seamlessly integrated within the corresponding PTO system, ensuring precise monitoring and control of the gyroscopic unit.

The ISWEC prototype is securely anchored in place using a hybrid spread mooring system. The configuration of the mooring system is depicted in Fig. 9 and consists of a symmetrical arrangement of four lines. Each mooring line is primarily composed of a polyester section, which provides structural strength, and a catenary section, which serves to prevent the polyester from making direct contact with the seabed and splash zone [26].

This hybrid mooring layout offers several advantages. By incorporating both jumper and catenary sections, the stiffness of the mooring lines is effectively reduced. This is crucial, as a fully taut mooring could have a significant impact on the pitch motion of the prototype and, consequently, affect the associated energy harvesting performance. The hybrid configuration allows for a more flexible and dynamic response, optimizing the device's ability to harness wave energy efficiently.

It is important to note that a mooring system is subject to various forces, which can be categorized as follows.

1) Mass-related forces: These forces arise from the inertial properties of the mooring line. The mass of the line contributes to its resistance to acceleration and deceleration, affecting the overall dynamics of the system.
2) Drag-related forces: These forces result from the relative velocity between the mooring line and the surrounding fluid. The drag force is influenced by factors such as the flow velocity, shape of the line, and surface roughness, and it impacts the behavior of the mooring system.
3) Stiffness-related forces: These forces can be further divided into two components.

a) Geometrical stiffness: This stiffness is associated with the geometry and configuration of the mooring line. It influences the response of the line to changes in position and shape, affecting the stability and motion of the system.
b) Axial stiffness: This stiffness relates to the axial properties of the mooring line, such as its material properties and cross-sectional area. It affects the resistance of the line to stretching or compression and plays a role in the overall structural behavior of the mooring system.

It is, indeed, challenging to achieve a scaled version of each force component when prototyping a mooring system. However, in the proposed experimental campaign, the axial stiffness is selected as the most influential force component in the system, and it is scaled accordingly. This choice is based on the understanding that the axial stiffness has a significant impact on the overall behavior of semitaut mooring systems.

By utilizing a semitaut configuration for the mooring, the polyester line primarily acts as a spring, contributing to the overall stiffness of the system. The resulting values of line stiffness are determined via experimental investigation, which provides insight into the behavior of the mooring under different conditions. Further details regarding the evaluation of line stiffness can be found in [31].

By carefully considering and scaling the axial stiffness, the prototype aims to replicate the behavior of the full-scale mooring system, hence providing valuable data for analysis and development.

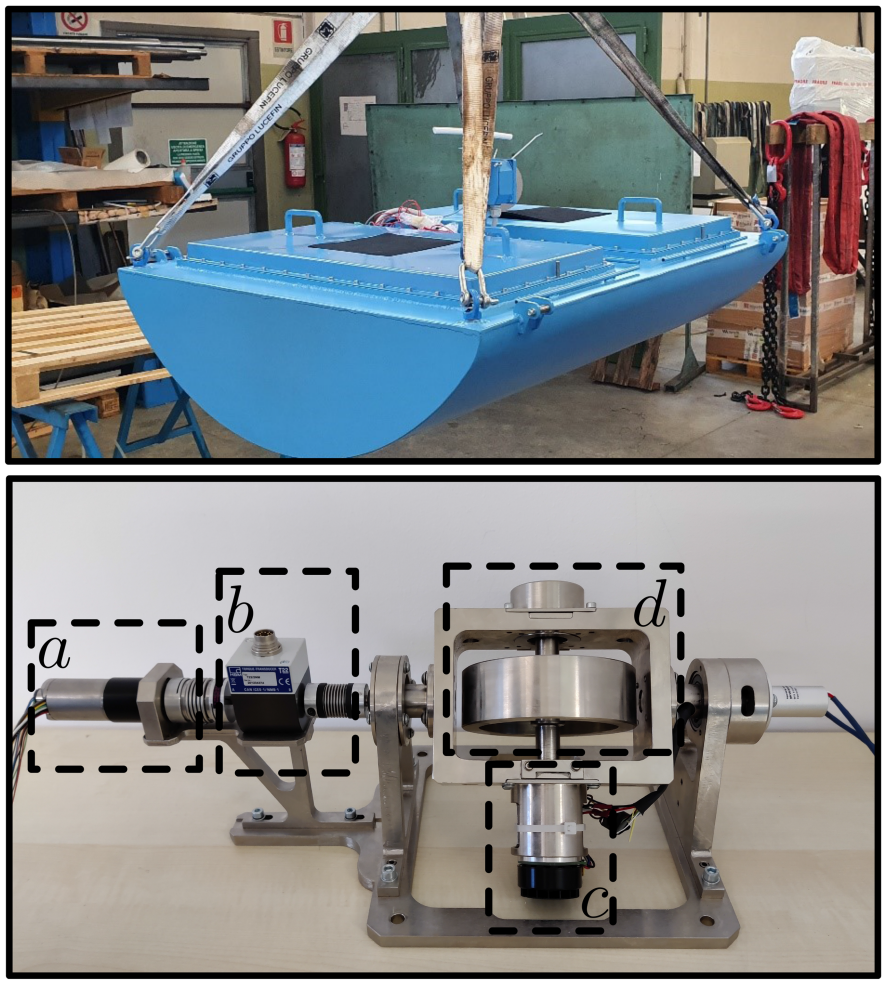


Fig. 8. On the top is the ISWEC prototype. On the bottom is the gyroscopic unit. $a$ is the gyroscope PTO, $b$ is the torque meter, $c$ is the flywheel motor, and $d$ is the flywheel.

## V. Validation of the Mathematical Models

Within this section, the validation process is described and structured according to the corresponding objectives of the experimental campaign, as outlined in Section IV-C.

It is important to note that calibration tests for each wave are conducted in undisturbed conditions, i.e., without the presence of the device in the wave tank. The purpose of these tests is to obtain the wave time history at the equilibrium position of the device. Subsequently, the wave time history is introduced within the numerical model, and the simulated results are compared to the experimental data.

This approach ensures that the calibration tests provide accurate reference data for validating the performance of the numerical model, replicating the corresponding wave conditions. The comparison between simulated and experimental data allows for an assessment of the reliability and accuracy of the numerical model in capturing the wave impact on the behavior of the device.

### A. Wave to Motion

Within this section, the waves are tested (in accordance with Table II) to validate the device kinematics, and therefore, the gyroscopic units are set into safety mode. The kinematic properties of the device are tested by evaluating the RAOs of the moored structure, i.e., by means of the Fourier transform of the device motion. In particular, the surge, heave, and pitch RAOs are evaluated and exposed, in magnitude, in Fig. 10. Thin lines in Fig. 10 refer to a single wave test; moreover, thick lines denote the average value of experimental and numerical tests, respectively. The black line is the BEM-based device response (which only includes the linear hydrodynamics of the device), and, hence, no mooring system is considered.

The numerical model response faithfully represents the dynamics of the prototype, considering the evident match between numerical and experimental RAOs. Additionally, note that the BEM response exhibits slight differences when compared to the experimental data, indicating that the mooring system has a minor, on average, influence on the dynamics of the unmoored system.

Furthermore, the numerical model adopted (as described in Section III) takes advantage of the inclusion of nonlinear slow varying wave forces. These forces can play a significant role in the evaluation of slow motions, such as that characterizing surge. Clearly, since the incoming wave has no significant frequency

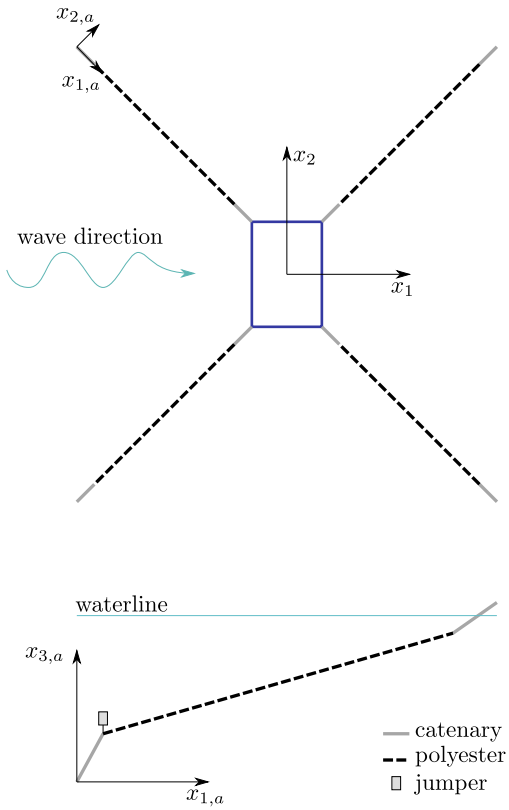


Fig. 9. Mooring configuration of the ISWEC prototype.

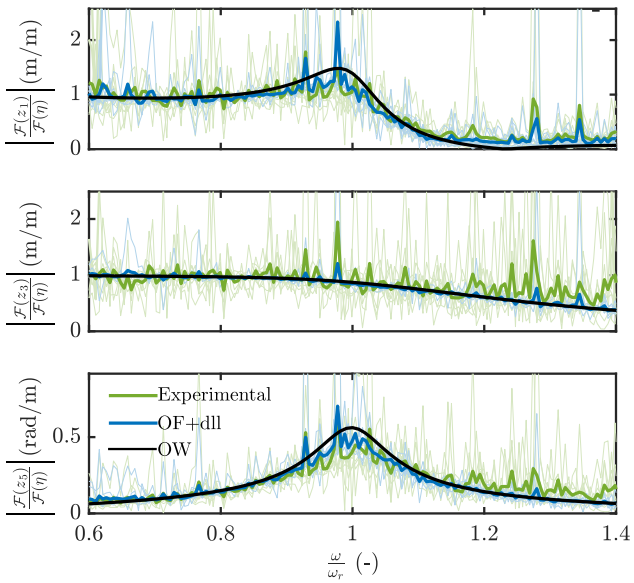


Fig. 10. ISWEC kinematic RAOs. The slim lines refer to any operative irregular condition tested and the bold lines refer to averaged values.

content within this range, the effect of drift forces cannot be appreciated within the experimentally computed RAO (note that the surge RAO is evaluated as $Z_1/\tilde{\eta}$, where no wave content means to "divide by zero"). Additionally, by examining the absolute value of the Fourier transform of the surge motion, it is possible to separate the frequency content of the signals

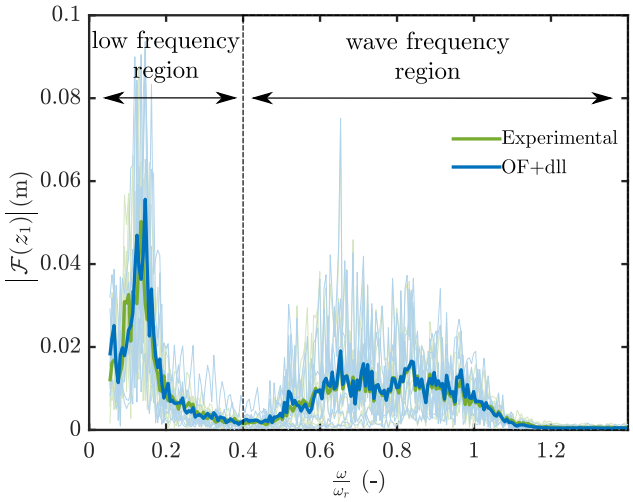


Fig. 11. ISWEC surge motion in the frequency domain. The slim lines refer to the operative irregular conditions tested while bold lines are used to denote average values.

into two regions. The high-frequency region corresponds to the presence of wave excitation forces while the low-frequency region corresponds to the presence of slowly varying forces.

To compare the surge motions between the numerical and experimental data in the frequency domain, Fig. 11 is included. It can be observed that the model accurately reproduces the experimental test results, particularly in the low-frequency region. This indicates that the developed model is capable of capturing the behavior of the surge motion across a range of frequencies, comprising the operational spectrum of the experimental WEC system.

For the sake of clarity, and according to the literature [32], it is well-established that the magnitude of the second-order wave force is lower than that of first-order forces. The significant motion amplitude observed in the surge direction is primarily caused by the resonance condition of the moored device. This resonance condition amplifies the response of the device to the wave excitation, resulting in a larger associated motion.

Although the tested waves can reach significant maximum heights (see Table II), it is important to validate the numerical models under extreme conditions. In harsh sea states, a real system can experience significant nonlinear forces [33]. For instance, Froude–Krylov forces, which are currently evaluated numerically using a linear BEM based on mean-wetted-area assumptions, can vary considerably due to changes in the waterline [34]. Additionally, other effects, such as slamming [8] and nonlinear restoring forces from the mooring system, can increase significantly in these rough conditions. Therefore, it is essential to assess the accuracy and reliability of the numerical models by comparing their predictions to experimental data under extreme sea states.

Despite the nonlinearities present in extreme conditions, the experimental response is accurately captured by the model, indicating that the nonlinear behavior associated with the wave's second-order forces is well-modeled (see Fig. 12). This demonstrates the model's ability to effectively capture and simulate

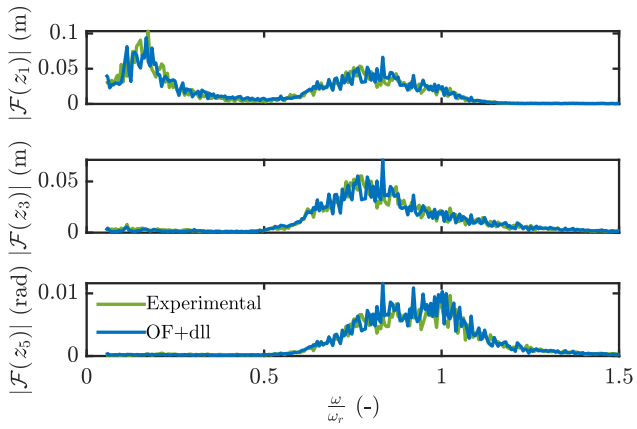


Fig. 12. Extreme wave, motion in the frequency domain.

TABLE IV
PITCH GOODNESS OF FIT (GOF) IN OPERATIVE IRREGULAR SEA STATES

| Wave identifier | NMSA $x_5$ |
|---|---|
| 01 irr | 0.92 |
| 02 irr | 0.82 |
| 03 irr | 0.72 |
| 04 irr | 0.89 |
| 05 irr | 0.89 |
| 06 irr | 0.77 |
| 07 irr | 0.74 |
| 08 irr | 0.83 |
| 09 irr | 0.83 |

the dynamics of the system even under extreme operating conditions.

Finally, the numerical model is compared to the experimental data in a time-domain fashion. Being the evaluation score between two signals defined as

$$\text{NMSA} = 1 - \frac{\|q - q^{\cdot}\|}{\|q - \mu_q\|} \tag{8}$$

with NMSA $\in \mathbb{R}$ the *normalized mean square accuracy*, and $\{q, q^{\cdot}\} \subset \mathbb{R}^m$ the reference and simulated signals, respectively. The model performance is offered in Table IV for the pitch motion.

Furthermore, a detailed analysis of the device motion time histories for wave 01 irr and wave 07 irr is provided in Fig. 13. These waves are selected to represent the best and worst matching conditions, respectively. It is evident that the device motion closely follows the expected behavior for wave 01 irr, indicating a good agreement between the experimental and numerical results. However, for wave 07 irr, the observed device motion deviates slightly from the expected response, suggesting a weaker match between the experimental and numerical data. This discrepancy can be attributed to the presence of nonlinearities, which become more pronounced with higher waves.

To gain a deeper understanding of the relationship between experimental data and the associated linear regression, Fig. 14 presents a scatter plot of the data points proportional to wave energy and wave height. The linear regression line provides an estimate of the expected device response. The Pearson correlation coefficient [35], which measures the strength and direction of the linear relationship between the variables, is calculated. The significant correlation observed indicates that wave energy and wave height have a considerable influence on the device motion, and the associated accuracy provided by the numerical model.

It is worth mentioning that correlation coefficients only measure linear relationships and, hence, do not capture nonlinear associations. Additionally, correlation does not imply causation, meaning that a strong correlation does not necessarily imply a cause-and-effect relationship between the variables.

### B. Wave to Gyro

Within this section, the validation process of the mechanism and, moreover, the response of the overall model, is investigated. Since the mechanism is subject to a corresponding control action, the associated controller design procedure is briefly described in the following.

*1) Control Synthesis for the ISWEC Prototype:* The system controller is designed by leveraging impedance-matching theory,[2] which is based on linear assumptions. However, when developing a small-scale prototype, uncertainties arise regarding the geometric and inertial properties of the individual components. As a result, a controller designed based on a white-box model of the full-scale device may not accurately represent the behavior of the prototype being investigated. These uncertainties highlight the need to carefully consider the differences between the full-scale system and the scaled-down prototype when designing the controller, taking into account the specific characteristics and limitations of the prototype. Under linear assumptions, the controlled system can be schematized as exposed in Fig. 15, in which, $\{F_\varepsilon, F_{\text{ctrl}}\} : \mathbb{R} \to \mathbb{C}^2, \omega \mapsto \{F_\varepsilon(\omega), F_{\text{ctrl}}(\omega)\}$ represent the force on the $\varepsilon$-axis, and the control action, respectively. $G_\varepsilon : \mathbb{R} \to \mathbb{C}^{2\times 2}, \omega \mapsto G_\varepsilon(\omega)$ represents the map of the controlled system, i.e., the system *seen* by the controller $K_{fb}$.

A set of tests during the experimental campaign has been performed with the aim of identifying the frequency response $G_\varepsilon$. By imposing a known, sufficiently exciting, signal ( i.e., a chirp signal in the ISWEC tests, see [38]) as the PTO torque, it is possible to evaluate the empirical transfer function estimate under investigation. Clearly, given the MIMO nature of the controlled system, the tests need to be performed for each controlled DoF, to identify each element of the frequency response $G_\varepsilon$, i.e.

$$G_\varepsilon = \begin{bmatrix} G_{\varepsilon,1,1} & G_{\varepsilon,1,2} \\ G_{\varepsilon,2,1} & G_{\varepsilon,2,2} \end{bmatrix} \tag{9}$$

[2]The reader is referred to the work in [36] and [37] for a detailed dissertation on the topic.

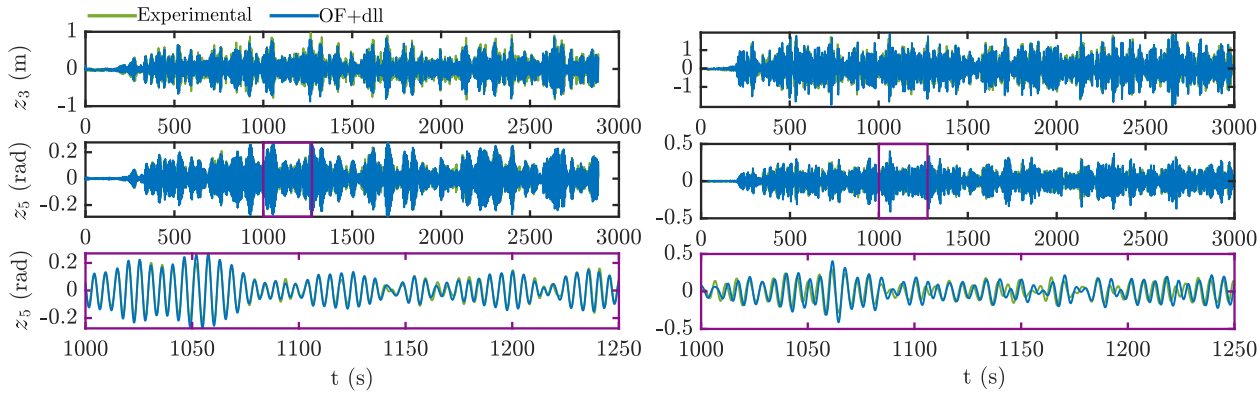


Fig. 13. Model time-domain comparison with experimental data. The wave 01 irr is exposed on the left-hand side of the picture as the best matching conditions. Viceversa, the wave 07 irr is exposed on the right-hand side of the picture as the worst matching conditions.

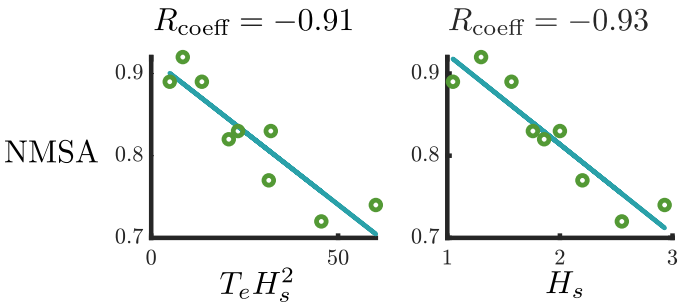


Fig. 14. Correlation between the evaluation score (NMSA) and the wave energy, on the left-hand side, and wave height, on the right-hand side. The correlation is evaluated numerically by means of the Pearson correlation coefficient $R_{\text{coeff}}$.

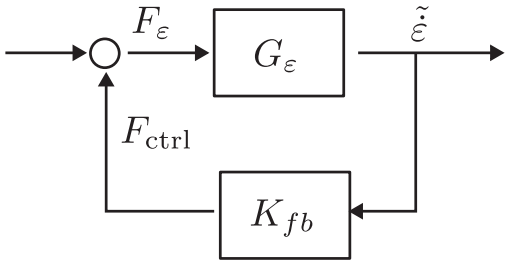


Fig. 15. Block diagram of the controlled LTI system.

in which $G_{\varepsilon,i,j} : \mathbb{R} \to \mathbb{C}, \omega \mapsto G_{\varepsilon,i,j}(\omega)$ can be evaluated as

$$G_{\varepsilon,i,j} = \frac{\tilde{\dot{\varepsilon}}_j}{F^{\text{ID}}_{\text{ctrl,i}}} \tag{10}$$

where $F^{\text{ID}}_{\text{ctrl,i}}$ represents the up-chirp control signal for the identification of the system, and $\{i, j\} \subset [1, 2]$.

The achieved experimental frequency response can be *visualized* by applying singular value decomposition to $G_\varepsilon$, in the so-called sigma plot [38] (see Fig. 16). Although the gyroscopic units should match perfectly, theoretically, some slight differences can be noted within the discussed responses, and hence, the matrix $G_\varepsilon$ is not symmetric.

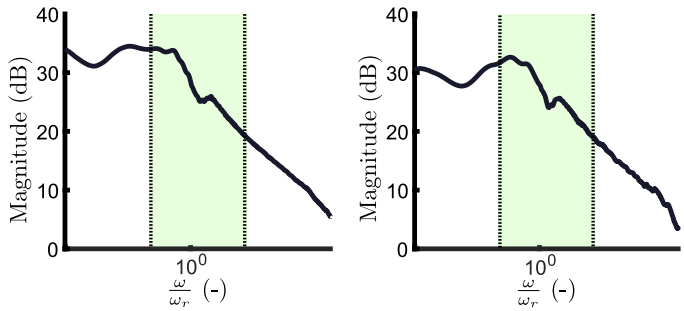


Fig. 16. Sigma plot of $G_\varepsilon$. The frequency operating region is highlighted in green. The sigma plot associated with the $\varepsilon_1$-axis is on the left, and the one associated with the $\varepsilon_2$-axis is on the right. Adapted from the work in [38].

The controller is synthesized within this experimental campaign by adopting a *proportional* (P), and a *proportional–integral* (PI) structure. Hence, the controller $K_{fb}$ can be written as

$$K_{fb}(s) = \begin{cases} \begin{bmatrix} k_{\theta,1,1} & k_{\theta,1,2} \\ k_{\theta,2,1} & k_{\theta,2,2} \end{bmatrix} & \text{if P} \\ \begin{bmatrix} \frac{sk_{p,1,1}+k_{i,1,1}}{s} & \frac{sk_{p,1,2}+k_{i,1,2}}{s} \\ \frac{sk_{p,2,1}+k_{i,2,1}}{s} & \frac{sk_{p,2,2}+k_{i,2,2}}{s} \end{bmatrix} & \text{if PI} \end{cases} \tag{11}$$

in which $\{k_\theta, k_p, k_i\} \subset \mathbb{R}^{2\times 2}$ are control parameters matrices relative to controller structures exposed in (11). Once the optimal controller response (which, according to the associated impedance-matching energy maximizing problem, can be computed as $K^{\text{opt}}_{fb} = G^{-*}_{\varepsilon}$) is defined, the controller structure $K_{fb}$ can be matched with the associated optimality conditions $K^{\text{opt}}_{fb}$ on a suitably chosen frequency. In particular, the frequency considered is associated with the energy period of a wave, i.e., $\omega_e = 2\pi/T_e$. For further information, the reader can refer to the work in [38].

*2) Experimental Tests and Model Validation:* The tests pursued within this validation are reported in Table V, with the

TABLE V
VALIDATING WAVES W2G

| test index | Wave identifier | controller | $\dot{\varphi}$ (r/min) |
|---|---|---|---|
| $w2g_1$ | 01 irr | $P$ | 225 |
| $w2g_2$ | 04 irr | $P$ | 225 |
| $w2g_3$ | 05 irr | $P$ | 225 |
| $w2g_4$ | 01 irr | $PI$ | 225 |

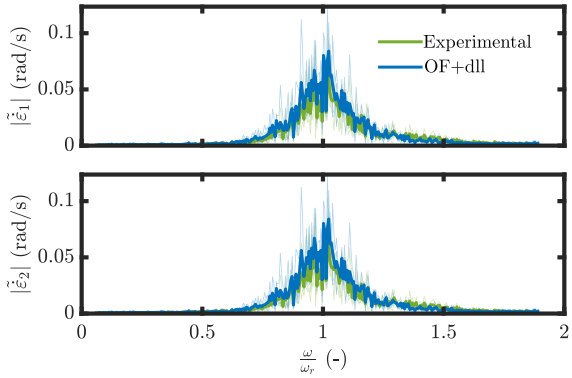


Fig. 17. Averaged empirical transfer function estimate magnitude of the PTOs axis velocity.

associated adopted control structure. Fig. 17 presents the corresponding comparison in the frequency domain. It is important to note that the results shown are the average values obtained from the entire set of waves in the same fashion as in Section V-A. The numerical model slightly overestimates the magnitude of the response compared to the experimental data. However, the model successfully captures the overall trend and frequency content of the experimental data. This indicates that, while there is some discrepancy in the magnitude, the model provides a reasonable representation of the system's behavior in terms of overall response.

In Fig. 18, the time histories of experimental and numerical tests for wave $w2g_4$ are presented. The numerical model successfully captures the overall behavior of the experimental device, demonstrating its effectiveness in replicating the system dynamics. However, a discrepancy arises when it comes to representing the friction of the small-scale prototype, particularly for small motions of the PTO axis.

The identification procedure of friction characteristics in mechanical systems involves an averaging process, which offers a single and effective model. However, this approach also has limitations, particularly when dealing with working conditions that exhibit a sufficiently large amplitude range. For a detailed discussion on this matter, refer to Section IV-B and Remark 2.

A time-domain appraisal is presented in Table VI. Despite the presence of nonlinearities, the model effectively captures the overall dynamics of the system. The errors observed can primarily be attributed to the challenging task of accurately

TABLE VI
GOF EVALUATED AS THE AVERAGE VALUE OF THE NMSE OF BOTH PTO AXIS SPEED

| test index | $\overline{\text{NMSA}}$ | | |
|---|---|---|---|
| | $z_5$ | $\dot{\varepsilon}_1$ | $\dot{\varepsilon}_2$ |
| $w2g_1$ | 0.871 | 0.748 | 0.731 |
| $w2g_2$ | 0.893 | 0.727 | 0.714 |
| $w2g_3$ | 0.912 | 0.785 | 0.773 |
| $w2g_4$ | 0.917 | 0.783 | 0.794 |

modeling the friction of the PTO axis, which has a significant influence on small-scale prototypes (see Section IV-B).

Additionally, the model demonstrates a good representation of the device pitch motion during this validation stage. It successfully captures the essential characteristics and behavior of the prototype, providing valuable insights into its performance.

### C. Wave to Tension

While the validation process of the moored system encompasses the analysis of its mechanical and hydrodynamic response, it is also important to examine the station-keeping system separately, especially under extreme conditions. In particular, specific aspects related to maintaining the position and stability of the device are thoroughly evaluated. This dedicated analysis ensures that the system remains robust and effective even in challenging scenarios, providing an additional level of validation and confidence in its performance.

It is important to note that the validation is primarily focused on extreme conditions due to limitations associated with the load cells used to measure tensions. The load cells may not accurately represent tensions under operational conditions, as their sensitivity is more suitable for higher tensions. Therefore, the validation efforts have been primarily directed toward extreme scenarios to ensure a thorough assessment of system performance.

Therefore, since the analysis in this section is related to the extreme wave tested, a statistical approach is pursued, as suggested by mooring design international standards [26].

According to the work in [26], the statistical response of a time series can be achieved by means of the so-called peak-over-threshold (POT) method in Fig. 19. Being the threshold defined as the average value of the signal, the maxima are sampled between the upcrossing and the successive downcrossing of the signal with the selected threshold.

The sampled maxima can be now fitted by means of an extreme distribution. According to the literature [39], [40], an extreme event is generally represented by means of three possible distribution functions, which are as follows:

1) type I: *Gumbel* distribution;
2) type II: *Fréchet* distribution;
3) type III: *Weibull* distribution.

The combination of these probability distribution defines the so-called *generalized extreme value distribution* (GEV distribution), i.e.

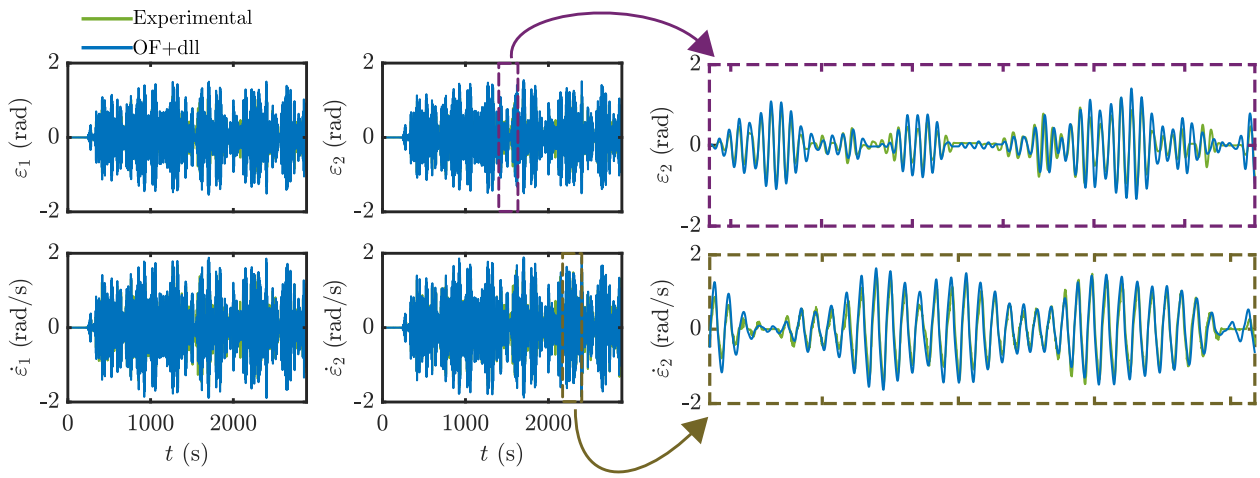


Fig. 18. Wave-to-gyro validation $w2g_4$. The yellow zoom plot shows the match between the numerical model and the experimental data and the purple one shows the friction behavior of the mechanical system.

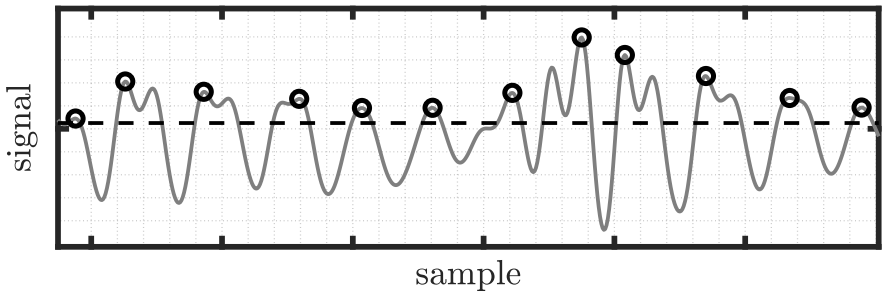


Fig. 19. Sampling of a signal maxima, the POT method.

$$\mathcal{P}(q) = \frac{1}{\sigma} p(q)^{\alpha+1} e^{-t(q)}$$

$$\mathcal{C}(q) = e^{-\left(1+\alpha\left(\frac{q-\mu}{\sigma}\right)\right)^{\frac{1}{\alpha}}} \tag{12}$$

in which $\{\mathcal{P}, \mathcal{C}\} : \mathbb{R} \to \mathbb{R}^+, q \mapsto \{\mathcal{P}(q), \mathcal{C}(q)\}$ represents the probability density function and the cumulative distribution function of the variable $q$, $\{\sigma, \mu, \alpha\} \subset \mathbb{R}$ are the three parameters of the GEV distribution, and $p : \mathbb{R} \to \mathbb{R}, q \mapsto p(q)$ is the map

$$p(q) = \begin{cases} \left(1 + \alpha \frac{q-\mu}{\sigma}\right) & \text{if} \quad \alpha \neq 0 \\ e^{-\frac{q-\mu}{\sigma}} & \text{if} \quad \alpha = 0. \end{cases} \tag{13}$$

The analysis is conducted using the GEV distribution, and the obtained results are presented in Fig. 20. The statistical model demonstrates a good fit to the experimental data. It is worth mentioning that the model is compared with the tension data acquired from one of the bow load cells, specifically $f_{lc,1}$. Additionally, the cumulative distribution function of the numerical model slightly overestimates the loads at the tail of the distribution. This indicates that the fitted model is conservative and provides a higher estimate of the loads compared to the experimental data.

As part of the process of establishing a representative model, the statistical models based on experimental data and numerical simulations are compared (see Fig. 21). The numerical-based model shows a good agreement with the experimental-based model. Additionally, there is a slight discrepancy in the tension values measured by the bow load cells during the experimental tests. It is important to note that since the problem is symmetric, with a planar wave and no excitation of roll, sway, and yaw motions, this slight discrepancy in the tension values measured by the bow load cells during the experimental tests can be attributed

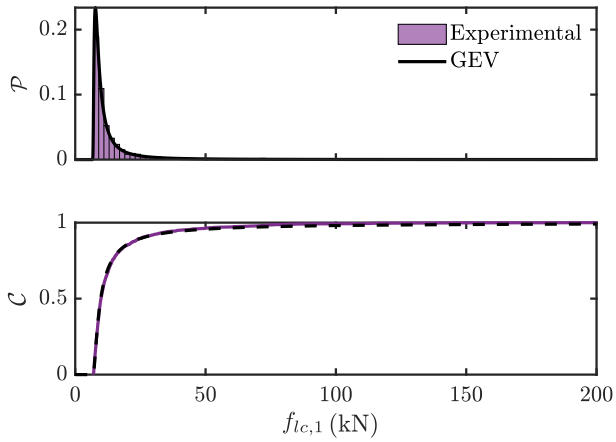


Fig. 20. Fitting of the GEV distribution on the experimental data. The probability density function is on the top, and the cumulative density function is on the bottom.

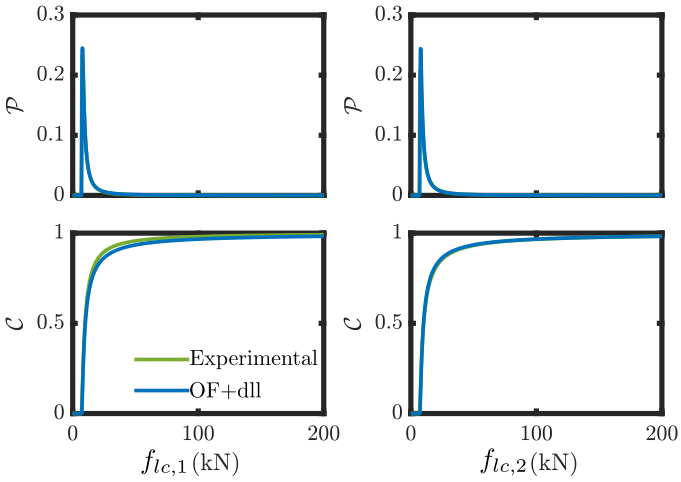


Fig. 21. Statistical data-based models. Comparison between experimental-generated and numerical-generated data.

to two possible factors. First, it could be caused by errors in the calibration stage of the load cells, where small inaccuracies in the measurement equipment or calibration procedure can lead to slight deviations in the measured values. Second, it is possible that the mooring system exhibits a slight asymmetric behavior, causing different tension readings in the bow load cells. This could be influenced by factors such as variations in the mooring line lengths or angles, or slight differences in the response of the mooring lines under load.

## VI. Numerical Investigation of the Moored ISWEC

As discussed in Section I, the resonant nature of wave energy devices pushes the commonly used hydrodynamic models, such as linear BEM software, beyond their assumptions. Additionally, the nonlinear behavior of mooring systems requires high-fidelity models for analysis. Accordingly, the validation achieved in Section V proved the model's reliability in capturing relevant dynamics in both operative and extreme conditions. As a result, by defining both a moored and unmoored layout, it becomes possible to assess the influence of the mooring system on device dynamics and its corresponding power performance. Furthermore, to provide an insight into the mooring influence on the ISWEC performances, the associated control synthesis plays a fundamental role.

The ISWEC is designed by leveraging a genetic-based algorithm [41] in which the geometry, the associated inertial properties, and the mechanism are optimized by means of a linearized model. Consequently, device performances are evaluated by synthesizing the control action (on a nonlinear model), defining, for any wave, with a PI controller structure, the associated parameters by means of gradient-based optimizations (see [24], for further information on the ISWEC developing tool). Accordingly, the control parameters are optimized by respecting the constraints imposed by technological limits (e.g., the maximum torque on the PTO axis). To investigate a large number of devices, the ISWEC developing tool overlooks the associated mooring system. Therefore, within this section, the numerical investigation on the influence of the station-keeping system on device performances is conducted, by analyzing the response of the validated model with and without the mooring system.

The site under investigation, on which performances of the device have been optimized, is Pantelleria (see Fig. 22). The associated scatter is discretized with a bin size of 0.25 s for the wave energetic period, and 0.2 m for the significant wave height, with a total number of 220 waves.

### A. Mooring Influence in Free Motion

The influence of the mooring system on the device's uncontrolled motion can play a fundamental role, not only in the assessment of device power-related performances but also in the design of such structures. For example, the maximum motion can be easily linked to some dimensioning phenomena, such as wave-in-deck forces and slamming, just to cite a few [29], [43], [44]. Accordingly, a device motion reduction can produce benefits in the design in terms of costs.

*Remark 3:* Note that, results are exposed herein as variation.

1) $\Delta_{\sigma_q} = 1 - (\sigma_{q,\text{unmoor}}/\sigma_{q,\text{moor}})$, in which $\{\sigma_{q,\text{unmoor}}, \sigma_{q,\text{moor}}\} \subset \mathbb{R}^+$ represents the standard deviation of the variable $q$ associated with the unmoored and moored layout, respectively.
2) $\Delta_{\max_q} = 1 - (\max_{q,\text{unmoor}}/\max_{q,\text{moor}})$, in which $\{\max_{q,\text{unmoor}}, \max_{q,\text{moor}}\} \subset \mathbb{R}^+$ represents the maximum value of the variable $q$ associated with the unmoored and moored layout, respectively.

According to the experimental investigation, surge and pitch motion are expected to be significantly restrained (see Fig. 10). Furthermore, the surge motion in moored and unmoored layouts cannot be compared[3] due to the surge zero-stiffness of the unmoored layout.

In Fig. 23, the results associated with the pitch motion are exposed. Device pitch motion is considerably restrained by the station-keeping system, with a maximum and mean variation in pitch motion of 24.8% and 14.5%, respectively. The nonlinearities associated with the mooring system, and the corresponding restoring forces on the device, rise according to the energetic content of a wave. It can be noted that, the mooring restoring force increases with the squared value of the wave height (see Remark 4).

*Remark 4:* The mooring restoring force on the device is highly influenced by the device offset (i.e., the distance from the equilibrium point, mainly affected by surge and sway motion), which is significantly influenced by the wave-related slow-varying forces (see [22], [32] for further information). These forces are expressed as a function of the squared wave amplitude.

In contrast with pitch motion, the heave is barely affected by the mooring system, with a maximum standard deviation variation of 1.4% (see Fig. 24).

[3]Note that, since the simulations are carried out in a time-domain fashion, the associated numerical analysis is accomplished by adopting synthetic data of each simulation (i.e., maximum value and/or standard deviation).

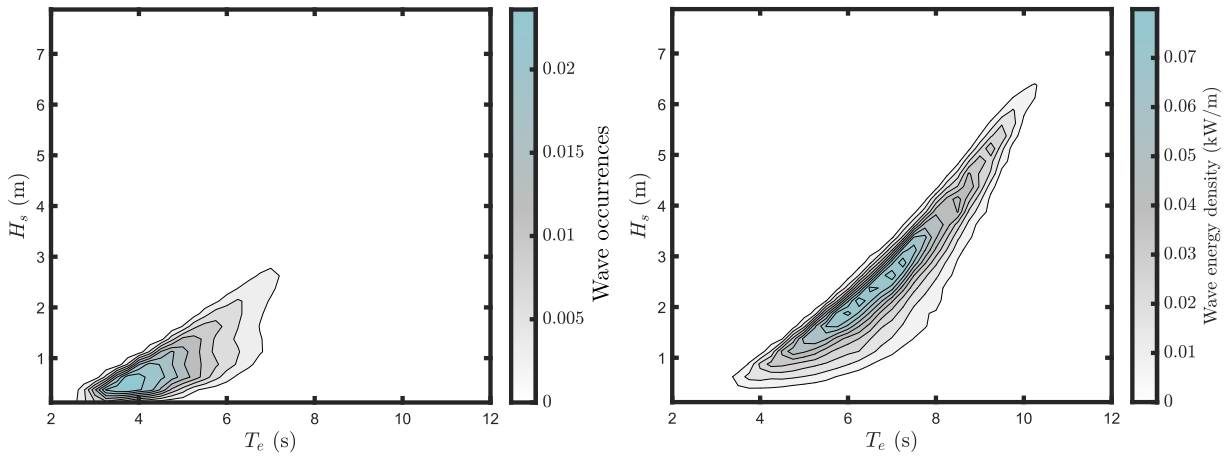


Fig. 22. Pantelleria energetic and occurrences scatters. Environmental data are downloaded by the ERA5 online database [42].

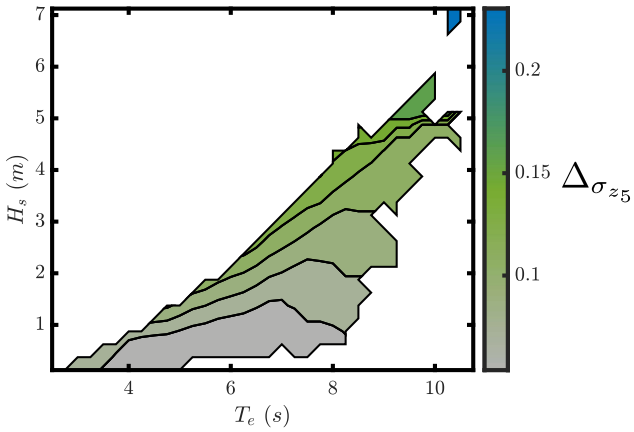


Fig. 23. Free motion: moored and unmoored model comparison. The variation of pitch motion standard deviation is exposed.

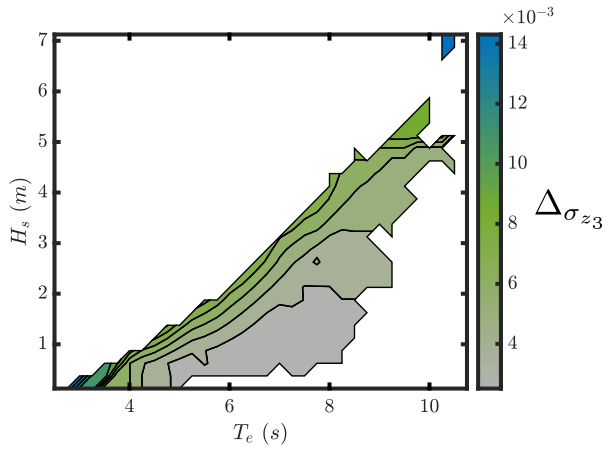


Fig. 24. Free motion: moored and unmoored model comparison. The variation of heave motion standard deviation is exposed.

### B. Mooring Influence in Controlled Conditions

The control action is optimized by means of numerical routines on the nonlinear unmoored model with nonlinearities related to the mechanism, and, therefore, the influence of the station-keeping system on the mechanical power can be estimated.

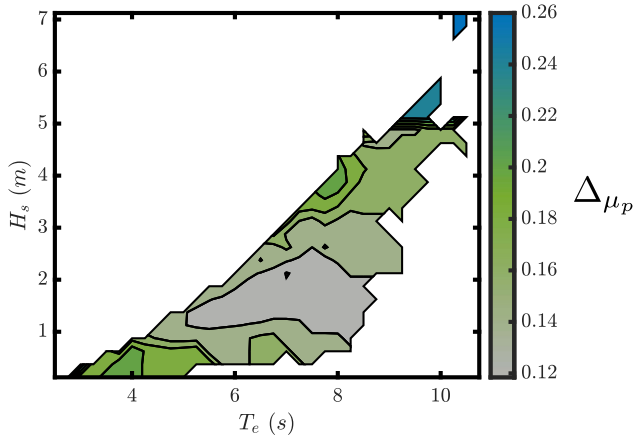


Fig. 25. Controlled conditions: moored and unmoored model comparison. The power mean value variation is exposed.

Moreover, the unmoored control action is optimized by respecting the real constraint on device PTO, i.e., by considering the following:

1) a maximum torque;
2) a torque standard deviation;
3) a maximum speed;
4) a speed standard deviation.

By analyzing these variables, it is possible to estimate the discrepancy between the control action obtained from the solution of the uncontrolled problem, and the actual control action that emerges when the mooring system is incorporated into the overall system dynamics.

Fig. 25 illustrates the significant influence of the station-keeping system on the mechanical power generated by the wave energy device. The mechanical power variation, denoted as $\Delta_{\mu_p}$, is calculated as the difference between the mechanical power obtained from the unmoored model ($\mu_{p,\text{unmoor}}$) and the mechanical power derived from the moored model ($\mu_{p,\text{moor}}$). This variation quantifies the deviation between the two models and highlights the impact of the mooring system on the overall power performance. The observed mechanical power variation,

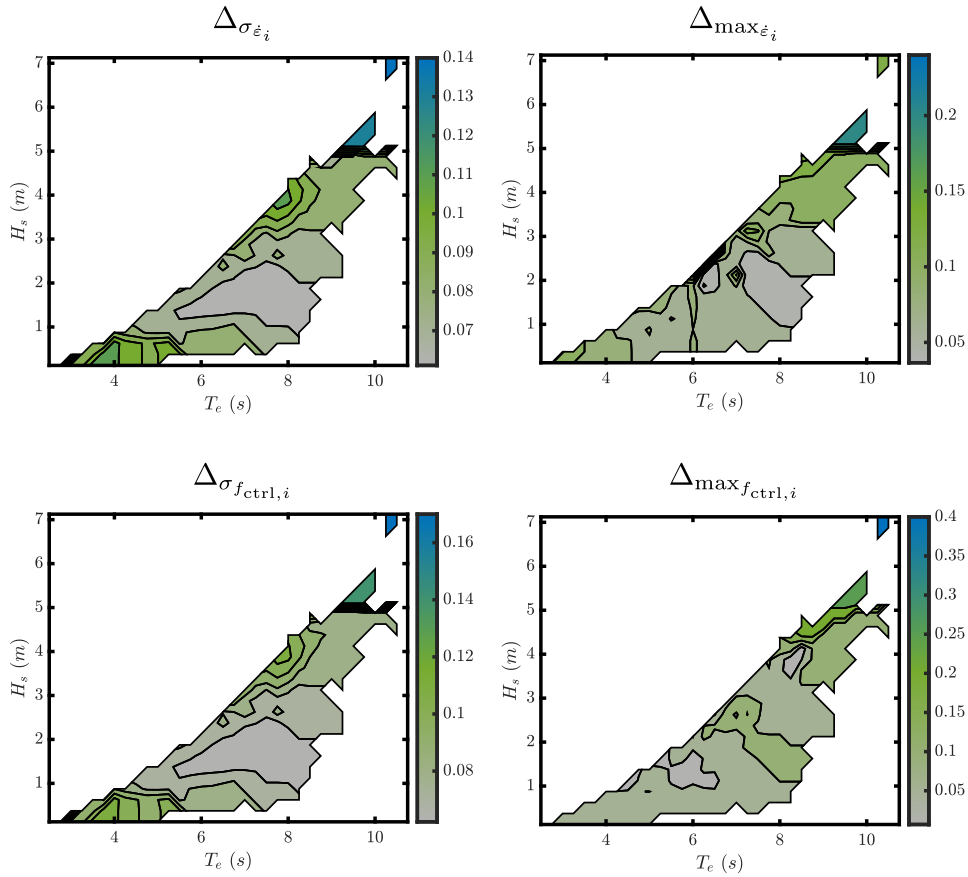


Fig. 26. Controlled conditions: moored and unmoored model comparison. On the top left-hand side, the $\dot{\varepsilon}_i$ standard deviation variation is exposed. On the top right-hand side, the $\dot{\varepsilon}_i$ maximum variation is exposed. On the bottom left-hand side, the control force standard deviation variation is exposed. On the bottom right-hand side, the control force maximum variation is exposed.

expressed as a percentage, provides valuable insights into the extent to which the inclusion of the mooring system affects the power generation capabilities of the wave energy device. This information is crucial for designing efficient and accurate control strategies that consider the influence of the mooring system on the WEC dynamics.

The analysis of the scatter plot reveals that the average variation in power output across the entire range of data points is approximately 19%, with a maximum value reaching 26%. These findings clearly indicate a significant impact of the mooring system on the performance of the ISWEC.

The influence of the mooring system on the controlled system response and the associated control action (i.e., $\dot{\varepsilon}_i$ and the associated control action $f_{\mathrm{ctrl},i}$, with $i \in \{1, 2\}$) is depicted in Fig. 26.[4]

From the figure, it is evident that the mooring system has a significant impact on both the controlled system response and the control action. The observed variations can be attributed to the nonoptimal control action computed using a numerical routine-based optimization for the unmoored model.

[4]Note that, within the numerical model, the gyroscopic units are identical, meaning that their responses are statistically equal ($\sigma_{\dot{\varepsilon}1} = \sigma_{\dot{\varepsilon}2}$), but in counterphase in the time-domain simulations.

Furthermore, the region highlighted in Fig. 25, where the power variation is lower (around 12%), can be explained by analyzing the control action in that region, which demonstrates considerable effectiveness even for the moored device. Overall, the diagram clearly shows the substantial influence of the mooring system, resulting in variations of up to 40% on the maximum control action. This highlights the necessity of including the mooring system in the control synthesis procedure.

## VII. Conclusion

Within the current offshore field, wave energy systems represent a novel application. However, the behavior of such devices exceeds the validity range of the most commonly used software, which relies on certain assumptions (e.g., small motion). While the hydrodynamics are often described in the literature using BEM software, the associated mooring system is generally overlooked due to its significant nonlinear nature and time-consuming numerical modeling.

To build a representative mathematical model, the first part of this study focuses on the experimental investigation of the ISWEC, a pitching wave energy system. The prototype is equipped with a gyroscopic mechanism and an associated controller. The validation is divided into three main sections: 1) analyzing the device motion, 2) the harvested energy, and 3)

the mooring tension. The validation process conducted demonstrates the model's fidelity from multiple perspectives. The proposed model successfully captures the hydrodynamics of the moored device, as evidenced in detail within this study. Additionally, the validation of the controlled systems reveals that while the accuracy indexes (i.e., NMSA) may be slightly lower in terms of mechanical response, the model remains accurate in representing the kinematics. This indicates that uncertainties related to the device mechanism, such as friction (see Remark 2), can pose challenges in scaled systems.

Overall, the results indicate that the numerical model effectively represents the dynamics of the device, both in free motion and under controlled conditions. Furthermore, in extreme sea states, the mooring tensions are well-described using a statistical approach.

The second part of the study focuses on conducting a numerical investigation to assess the influence of the mooring system on the dynamics of the overall system. This analysis involves examining the system scatter, which provides insights into the system response under various conditions. The results demonstrate that the mooring system plays a crucial role and has a notable impact on the system response, both in controlled and uncontrolled conditions. Furthermore, when the mooring dynamics are integrated into the model, a significant reduction in harvested power is observed, with an average decrease of 19%.

In conclusion, the findings of this study clearly demonstrate that the mooring system has a substantial impact on the dynamics of the wave energy device. This highlights the inadequacy of using an unmoored model to calculate the corresponding control action, as it does not accurately represent the system behavior. Therefore, it is essential to incorporate the station-keeping system into the controller synthesis process. By including the mooring dynamics in the controller design, the system will be able to effectively account for the influence of the mooring system, leading to improved performance and optimized energy extraction.

## References


[1] IEA, IRENA, UNSD, World Bank, and WHO, "Tracking SDG 7: The energy progress report," 2023. [Online]. Available: http://trackingsdg7.esmap.org/

[2] A. T. González, P. Dunning, I. Howard, K. McKee, and M. Wiercigroch, "Is wave energy untapped potential?," *Int. J. Mech. Sci.*, vol. 205, 2021, Art. no. 106544. [Online]. Available: https://www.sciencedirect.com/science/article/pii/S0020740321002794

[3] G. M. J. Herbert, S. Iniyan, E. Sreevalsan, and S. Rajapandian, "A review of wind energy technologies," *Renewable Sustain. Energy Rev.*, vol. 11, pp. 1117–1145, 2007. [Online]. Available: https://www.sciencedirect.com/science/article/pii/S136403210500095X

[4] O. Ellabban, H. Abu-Rub, and F. Blaabjerg, "Renewable energy resources: Current status, future prospects and their enabling technology," *Renewable Sustain. Energy Rev.*, vol. 39, pp. 748–764, 2014.

[5] P. Zhang, W. Li, S. Li, Y. Wang, and W. Xiao, "Reliability assessment of photovoltaic power systems: Review of current status and future perspectives," *Appl. Energy*, vol. 104, pp. 822–833, 2013. [Online]. Available: https://www.sciencedirect.com/science/article/pii/S0306261912008926

[6] I. López, J. Andreu, S. Ceballos, I. M. D. Alegría, and I. Kortabarria, "Review of wave energy technologies and the necessary power-equipment," *Renewable Sustain. Energy Rev.*, vol. 27, pp. 413–434, 2013.

[7] M. Herrando, A. Coca-Ortegón, I. Guedea, and N. Fueyo, "Experimental validation of a solar system based on hybrid photovoltaic-thermal collectors and a reversible heat pump for the energy provision in non-residential buildings," *Renewable Sustain. Energy Rev.*, vol. 178, 2023, Art. no. 113233.

[8] M. Penalba, G. Giorgi, and J. V. Ringwood, "A review of non-linear approaches for wave energy converter modelling," in *Proc. 11th Eur. Wave Tidal Energy Conf.*, 2015.

[9] N. Pozzi, M. Bonfanti, and G. Mattiazzo, "Mathematical modeling and scaling of the friction losses of a mechanical gyroscope," *Int. J. Appl. Mech.*, vol. 10, no. 3, 2018, doi: 10.1142/S1758825118500242.

[10] F. Niosi et al., "Experimental validation of OrcaFlex-based numerical models for the PEWEC device," *Ocean Eng.*, vol. 281, 2023, Art. no. 114963.

[11] B. Fenu, M. Bonfanti, A. Bardazzi, C. Pilloton, A. Lucarelli, and G. Mattiazzo, "Experimental investigation of a multi-OWC wind turbine floating platform," *Ocean Eng.*, vol. 281, 2023, Art. no. 114619.

[12] B. Paduano, E. Pasta, G. Papini, F. Carapellese, and G. Bracco, "Mooring influence on the productivity of a pitching wave energy converter," in *Proc. OCEANS*, 2021, pp. 1–6.

[13] B. Paduano, P. Edoardo, N. Faedo, and G. Mattiazzo, "Control synthesis via impedance-matching in panchromatic conditions: A generalised framework for moored systems," in *Proc. Eur. Wave Tidal Energy Conf.*, 2023, p 344, doi: 10.36688/ewtec-2023-344.

[14] B. Paduano, F. Carapellese, E. Pasta, N. Faedo, and G. Mattiazzo, "Optimal controller tuning for a nonlinear moored wave energy converter via non-parametric frequency-domain techniques," *Renew*, 2022, doi: 10.1201/9781003360773-45.

[15] B. Paduano, F. Carapellese, E. Pasta, S. Sergej, N. Faedo, and G. Mattiazzo, "Data-based control synthesis and performance assessment for moored wave energy conversion systems: The PeWEC case," *IEEE Trans. Sustain. Energy*, vol. 15, no. 1, pp. 355–367, Jan. 2024.

[16] B. Tagliafierro et al., "A numerical study of a taut-moored point-absorber wave energy converter with a linear power take-off system under extreme wave conditions," *Appl. Energy*, vol. 311, 2022, Art. no. 118629.

[17] B. Paduano et al., "Control co-design mooring optimisation for wave energy systems: A three-tethered point absorber case," *IFAC-PapersOnLine*, vol. 56, no. 2, pp. 11717–11722, 2023, doi: 10.1016/j.ifacol.2023.10.537. [Online]. Available: https://www.sciencedirect.com/science/article/pii/S2405896323009047

[18] G. Papini, B. Paduano, E. Pasta, F. Carapellese, G. Mattiazzo, and N. Faedo, "On the influence of mooring systems in optimal predictive control for wave energy converters," *Renewable Energy*, vol. 218, 2023, Art. no. 119242. [Online]. Available: https://linkinghub.elsevier.com/retrieve/pii/S0960148123011576

[19] G. Bracco, "ISWEC: A gyroscopic wave energy converter," 2010. [Online]. Available: http://porto.polito.it/id/eprint/2562362

[20] *Orcina*, "OrcaFlex manual," 2020. [Online]. Available: www.orcina.com

[21] J. Davidson and J. V. Ringwood, "Mathematical modelling of mooring systems for wave energy converters—A review," *Energies*, vol. 10, pp. 1188–1207, 2017.

[22] J. M. J. Journee and W. W. Massie, *Offshore Hydromechanics*, 1st ed. Delft, The Netherlands: Delft Univ. Technol., 2001.

[23] W. E. Cummins, "The impulse response function and ship motions," *Schiffstechnik*, vol. 9, pp. 101–109, 1962.

[24] S. A. Sirigu et al., "ISWEC design tool," *Int. J. Mar. Energy*, vol. 15, pp. 201–213, 2016.

[25] J. Na, Q. Chen, and X. Ren, "Chapter 1 - Friction dynamics and modeling," 2018. [Online]. Available: https://www.sciencedirect.com/science/article/pii/B9780128136836000039

[26] DNV, "DNV-OS-E301 position mooring," 2015. [Online]. Available: www.dnvgl.com

[27] M. Bonfanti, S. A. Sirigu, G. Giorgi, P. Dafnakis, G. Bracco, and G. Mattiazzo, "A passive control strategy applied to the ISWEC device: Numerical modelling and experimental tests," *Int. J. Mechanics Control*, vol. 21, pp. 143–154, 2020.

[28] M. Bonfanti and G. Giorgi, "Improving computational efficiency in WEC design: Spectral-domain modelling in techno-economic optimization," *J. Mar. Sci. Eng.*, vol. 10, no. 10, p. 1468, 2022, doi: 10.3390/jmse10101468.

[29] Det Norske Veritas, "Environmental conditions and environmental loads," 2019. [Online]. Available: https://www.dnv.com/oilgas/download/dnv-rp-c205-environmental-conditions-and-environmental-loads.html

[30] M. Bonfanti and S. A. Sirigu, "Spectral-domain modelling of a non-linear wave energy converter: Analytical derivation and computational experiments," *Mech. Syst. Signal Process.*, vol. 198, 2023, Art. no. 110398.

[31] S. A. Sirigu, M. Fontana, and B. Paduano, "Experimental identification of synthetic ropes stiffness for scaled mooring systems," in *Advances in Italian Mechanism Science. IFToMM Italy 2022. Mechanisms and Machine Science*, V. Niola, A. Gasparetto, G. Quaglia, and G. Carbone, Eds. Berlin, Germany: Springer, 2022, pp. 891–899.

[32] O. Faltinsen, *Sea Loads on Ships and Offshore Structures*. New York, NY, USA: Cambridge Univ. Press, 1993.

[33] M. Penalba, G. Giorgi, and J. V. Ringwood, "Mathematical modelling of wave energy converters: A review of nonlinear approaches," *Renewable Sustain. Energy Rev.*, vol. 78, pp. 1188–1207, 2017.
[34] G. Giorgi and J. V. Ringwood, "Nonlinear Froude-Krylov and viscous drag representations for wave energy converters in the computation/fidelity continuum," *Ocean Eng.*, vol. 141, pp. 164–175, 2017.
[35] K. Pearson, "Note on regression and inheritance in the case of two parents," *Proc. Roy. Soc. London*, vol. 58, pp. 240–242, 1895.
[36] T. L. Floyd and E. Pownell, *Principles of Electric Circuits*. Noida, India: Pearson India, 2000.
[37] N. Faedo, F. Carapellese, E. Pasta, and G. Mattiazzo, "On the principle of impedance-matching for underactuated wave energy harvesting systems," *Appl. Ocean Res.*, vol. 118, 2022, Art. no. 102958.
[38] N. Faedo et al., "Energy-maximising experimental control synthesis via impedance-matching for a multi degree-of-freedom wave energy converter," in *Proc. 14th IFAC Conf. Control Appl. Mar. Syst. Robot. Veh.*, 2022, pp. 345–350.
[39] Cláudia Alves Isabel Fraga Neves, "Extreme value distributions," *Int. Encyclopedia Statist. Sci.*, Miodrag Lovric Ed., Berlin, Heidelberg: Springer Berlin Heidelberg, pp. 493–496, 2011, doi: 10.1007/978-3-642-04898-2_246.
[40] M. Jacob, C. Neves, and D. V. Greetham, *Forecasting and Assessing Risk of Individual Electricity Peaks*. Cham, Switzerland: Springer, 2020, doi: 10.1007/978-3-030-28669-9.
[41] F. Carapellese, S. A. Sirigu, G. Giorgi, M. Bonfanti, and G. Mattiazzo, "Multiobjective optimisation approaches applied to a wave energy converter design," 2021. [Online]. Available: https://www.scopus.com/inward/record.uri?eid=2-s2.0-85120051235&partnerID=40&md5=e7a1155d1e59a744890eb939bc4a5d20
[42] H. Hersbach et al., "The ERA5 global reanalysis," *Quart. J. Roy. Meteorol. Soc.*, vol. 146, pp. 1999–2049, 2020.
[43] Det Norske Veritas, "Design of offshore steel structures, general - LRFD method," 2011. [Online]. Available: https://rules.dnv.com/docs/pdf/dnvpm/codes/docs/2011-04/Os-C101.pdf
[44] RINA, "Regolamenti per la classificazione delle navi - Parte B," 2005. [Online]. Available: https://www.rina.org/en/rules

**Bruno Paduano** was born in Pompei, Italy, in 1992. He received the M.Sc. and Ph.D. degrees in mechanical engineering from Politecnico di Torino, Turin, Italy, in 2019 and 2023, respectively.

He is currently a Researcher with Marine Offshore Renewable Energy Lab, Politecnico di Torino, with a focus on system identification techniques for moored wave energy converters. In 2022, he was a Visiting Researcher with WaveEC Offshore Renewables, Lisbon. His research interests include device survivability, experimental testing, model validation, and control synthesis within high-fidelity models.

**Fabio Carapellese** was born in Andria, Italy, in 1995. He received the B.Sc. degree in mechanical engineering and the M.Sc. degree in mechatronic engineering from Politecnico di Torino, Turin, Italy, in 2017 and 2019, respectively. He received the Ph.D. degree in mechanical engineering with the research on a novel omnidirectional wave energy technology at the Marine Offshore Renewable Energy Lab, Politecnico di Torino, Turin, Italy. His doctoral thesis focuses on the dynamic design of multi-degree-of-freedom WEC systems, with a particular emphasis on their nonlinear behavior.

In 2022, he was a Visiting Researcher with the Wallace Energy Systems and Renewables Facility, Oregon State University, Corvallis (OR), U.S. His current research interests include the advancing of the modeling and control techniques for actuated flexible systems, exploring their practical applications within wave energy systems.

In 2022, he was a recipient of the 2022 IFAC CAMS Best Paper Award.

**Edoardo Pasta** (Graduate Student Member, IEEE) was born in Turin, Italy, in 1996. He received the B.Sc. degree in mechanical engineering and the M.Sc. degree in mechatronic engineering in 2018 and 2020, respectively, from Politecnico di Torino, Turin, where he is currently working toward the Ph.D. degree in mechanical engineering with a focus on optimal control and modeling of wave energy converters, with Marine Offshore Renewable Energy Lab.

In 2020, he was a Visiting Researcher with Computational Fluid Dynamics and Flow Physics Laboratory, San Diego State University, San Diego, CA, USA. Between 2021 and 2022, he joined the Centre for Ocean Energy Research, Maynooth University, Ireland, as a Visiting Researcher. His current research interests include optimal control and modeling of wave energy systems, with a particular focus on data-based and data-driven techniques.

Mr. Pasta was a recipient of the 2022 IFAC CAMS Best Paper Award in 2022.

**Mauro Bonfanti** was born in Crema, Italy, in 1992. He received the B.Sc. degree in mechanical engineering from the Politecnico di Milano, Milan, Italy, in 2014, and the M.Sc. and Ph.D. degrees in mechanical engineering from the Politecnico di Torino, Turin, Italy, in 2016 and 2021, respectively.

He is currently an Academic Researcher (RTDA) with the Politecnico di Torino, with a focus on wave energy conversion systems, hydrofoil-equipped boats, autonomous navigation applied to the waterborne mobility, and zero-emission hybrid propulsion systems for marine vessels.

**Sergej Antonello Sirigu** was born in 1990. He received the master's and Ph.D. degrees in mechanical engineering from the Politecnico di Torino, Turin, Italy, in 2015 and 2019, respectively.

He is currently a nontenured track Assistant Professor with MOREnergy Lab, Politecnico di Torino. With over eight years of experience, he has focused his research and development efforts on offshore marine renewable technologies. His current research interests include numerical modeling and experimental testing of wave energy converters, robust techno-economic optimization, and the design of large modular floating structures.

**Dario Basile** received the bachelor degree in chemical engineering and master's degree in chemical engineering from Università degli Studi di Napoli "Federico II", in 2017 and 2019, respectively, and a second-level master's degree in energy innovation from Politecnico di Milano in 2020.

He is currently an R&D Project Manager with Eni's Facilities, Wind and Marine Energy Research Center, San Donato Milanese, Italy. After working experience in Eni's O&G Production Engineering Department, he is currently involved in the development of innovative subsea production systems and marine energy projects, such as inertial sea wave energy converter technology.

**Domenica Pizzirusso** was born in Avellino, Italy, in 1989. She received the bachelor degree in naval engineering and master's degree in naval engineering from Università degli Studi di Napoli "Federico II", in 2012 and 2014, respectively, and a second-level master's degree in design of Oil & Gas plants from Alma Mater Studiorum - Universit di Bologna in 2015.

She is currently a Senior Naval Architect with EniProgetti Milan, San Donato Milanese MI, Italy. She is currently involved in both the development of naval design of Oil&Gas assets and in marine energy projects, such as inertial sea wave energy converter technology.

**Nicoláas Faedo** was born in Buenos Aires, Argentina, in 1991. He received the degree in automation and control engineering from the National University of Quilmes, Buenos Aires, in 2015, and the Ph.D. degree in electronic engineering from the Centre for Ocean Energy Research Group, Maynooth University, Kildare, Ireland, in 2020, with a focus on optimal control and model reduction for wave energy converters from a system-theoretic perspective.

In 2017, he joined the Centre for Ocean Energy Research Group, Maynooth University. He was a Visiting Researcher multiple times with the Control and Power Group, Imperial College London, London, U.K., in 2018. He currently holds a postdoctoral position with the Department of Mechanical and Aerospace Engineering, Politecnico di Torino, Turin, Italy. His current research interests include nonlinear optimal control theory and data-driven model reduction, with special emphasis on applications involving renewable energy systems.

Dr. Faedo is the recipient of a Marie Skłodowska-Curie Actions Individual Fellowship (MSCA-IF 2020). He was a recipient of the 2022 IFAC CAMS Best Paper Award, the 2019 ISOPE Best Student Paper Award, and the Exxonmobile Prize, the finalist for the 2018 IFAC CAMS Young Author Award, and has been selected an Outstanding Reviewer two years in a row from 2020 to 2021 for the IEEE TRANSACTIONS ON SUSTAINABLE ENERGY.

**Giuliana Mattiazzo** received the M.Sc. degree in aerospace engineering and the Ph.D. degree in applied mechanics from the Politecnico di Torino, Turin, Italy, in 1991 and 1994, respectively.

She is currently a Full Professor with the Department of Mechanical and Aerospace Engineering, Politecnico di Torino, where she is also the Vice-Rector for Technology Transfer and the Director of the Marine Offshore Renewable Energy Lab. Her research interests include renewable energy applications, with a particular focus on the development of wave energy converters, floating offshore wind plants, and decarbonization strategies for local energy communities.

Open Access funding provided by 'Politecnico di Torino' within the CRUI CARE Agreement